Heterogeneity of the Ailaoshan–Song Ma ophiolitic mélange and their palaeogeographic implications for the evolution of Eastern Palaeo-Tethys

Fei Liu, Wei Lin, Yin Wang, Lingtong Meng, Michel Faure, Vuong van Nguyen, Qinying Wu, Yang Chu, Wei Wei, Hoai Luong Thi Thu, et al.

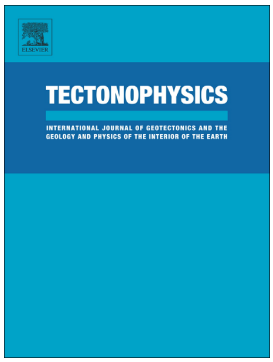

Heterogeneity of the Ailaoshan–Song Ma ophiolitic mélange and their palaeogeographic implications for the evolution of Eastern Palaeo-Tethys

Fei Liu, Wei Lin, Yin Wang, Lingtong Meng, Michel Faure, Vuong Van Nguyen, Qinying Wu, Yang Chu, Wei Wei, Hoai Luong Thi Thu, Tich Van Vu, Qiuli Li, Hao Wang, Ke Chen

PII: S0040-1951(23)00146-4

DOI: https://doi.org/10.1016/j.tecto.2023.229848

Reference: TECTO 229848

To appear in: *Tectonophysics*

Received date: 30 November 2022

Revised date: 2 April 2023

Accepted date: 4 April 2023

Please cite this article as: F. Liu, W. Lin, Y. Wang, et al., Heterogeneity of the Ailaoshan–Song Ma ophiolitic mélange and their palaeogeographic implications for the evolution of Eastern Palaeo-Tethys, *Tectonophysics* (2023), https://doi.org/10.1016/j.tecto.2023.229848

Heterogeneity of the Ailaoshan–Song Ma ophiolitic mélange and their palaeogeographic implications for the evolution of Eastern Palaeo-Tethys

Fei Liu [a,b,c], Wei Lin [a,b] *, Yin Wang [a,b], Lingtong Meng [a,b], Michel Faure [d], Vuong Van Nguyen [e], Qinying Wu [a,b], Yang Chu [a,b], Wei Wei [a,b], Hoai Luong Thi Thu [e], Tich Van Vu [e], Qiuli Li [a,b], Hao Wang [a,b], Ke Chen [a,b]

a State Key Laboratory of Lithospheric Evolution, Institute of Geology and Geophysics, Innovation Academy of Earth Science, Chinese Academy of Sciences, Beijing 100029, China

b College of Earth and Planetary Sciences, University of Chinese Academy of Sciences, Beijing 100049, China

c Wuhan Center of China Geological Survey (Central South China Innovation Center for Geosciences), Wuhan 430205, China

d Institut des Sciences de la Terre d'Orléans, UMR CNRS 7327, Université d'Orléans, 45067 Orléans Cedex 2, France

e University of Science, Vietnam National University, Hanoi, Viet Nam

f Oil and Gas Resources Survey Center, China Geological Survey, Beijing 100029, China

* Corresponding author.

E-mail addresses: linwei@mail.iggcas.ac.cn (W. Lin).

Abstract

In comparison with ophiolite, the ophiolitic mélange, especially its matrix, contains more information about the evolution of the relevant ocean. The evolution of the eastern Palaeo-Tethys recorded a whole Wilson cycle of numerous continental blocks such as the South China Block and Indochina Block, including rifting away from the Gondwana continent, subsequent northward migration and final collage with the Laurasia continent. Based on structural geology, detrital zircon, and related geochemical analyses, the Ailaoshan–Song Ma ophiolitic mélange can be divided into M1, M2, and M3 units with distinct detrital zircon age spectra and $\varepsilon_{Hf}(t)$ values suggesting for different provenances. These units are in faults-contact along the orogenic belt, indicating a strike–parallel heterogeneity of the ophiolitic mélange. To further understand the heterogeneity of these ophiolitic mélanges, five samples from the matrix of the Ailaoshan ophiolitic mélange were collected to be conducted detrital zircon U–Pb dating and Lu–Hf isotope analyses. All samples share the same zircon age spectrum, with two obvious age peaks at 430 and 960 Ma, which is comparable with the M1 unit. These results imply that the northwestern Ailaoshan ophiolitic mélange segment can be subdivided into M1 in the interior and M2 in the exterior rather than the previous division, indicating a strike–perpendicular heterogeneity. Based on their geometries (NE-dipping) and depositional ages (M1, 310–270 Ma; M2, 260–240 Ma), the elder M1 unit was thrusted upon the younger M2 unit, indicating a tectonic inversion. This inversion, which is associated with the whole geometry of the Ailaoshan belt, is ascribed to the transpressive deformation of the Cenozoic Red River Fault. These spatial heterogeneities well match the different evolutionary stages of the

eastern Palaeo-Tethys.

Keywords: Ailaoshan–Song Ma orogenic belt, Matrix of the ophiolitic mélange, Detrital zircon, In-situ Hf isotopic content, Spatial heterogeneity, Eastern Palaeo-Tethys

1 Introduction

The ophiolitic mélanges represent remnants of a vanished oceanic lithosphere. They are often regarded as the suture zones between two continental blocks (Hess, 1955; Coleman, 1977; Dewey, 1977, 2005; Smith and Colchen, 1988; Şengör, 1992). They may also receive materials derived from obducted and subducted blocks and oceanic plate strata. Therefore, ophiolitic mélanges are critical for understanding the evolution of the disappeared ocean (Harris et al., 1998; Festa et al., 2010, 2012; Dilek and Furnes, 2011; Li et al., 2021; Wang et al., 2021). Generally, the ophiolitic mélanges are composed of exotic blocks (ultramafic rocks, mafic rocks, cherts and volcanic rocks) and matrix (turbidites and pebbly mudstone), showing a "block-in-matrix" structure (Festa et al., 2010, 2012). Although these blocks have been widely applied to determine the formation age of ophiolites (Mukasa and Ludden, 1987), the ages obtained have been limited and they cannot be used to

rebuild the long-lasting evolutionary history of the ocean (Lin et al., 2022). However, the matrices of the ophiolitic mélanges can record the long-term evolutionary history of the ocean owing to their sensitive responses to tectonic events, and variable components and provenances (Harris et al., 1998; Li et al., 2021; Wang et al., 2021; Lin et al., 2022). In this respect, detrital zircons are useful in the provenance analysis owing to their physicochemical resistance and high concentrations of certain key trace elements (Fedo, 2003; Cawood et al., 2012; Lin et al., 2018; Chu et al., 2021).

The Ailaoshan–Song Ma ophiolitic mélange is proposed as the suture zone between the South China Block (SCB) and Indochina Block (IB) (Fig. 1). However, the evolution of the Ailaoshan–Song Ma Ocean, which is generally interpreted as a branch of the eastern Palaeo-Tethys, has not yet been well documented, and significant scientific issues remain disputed (Lepvrier et al., 1997; Zhong, 1998; Chen et al., 2014; Xia et al., 2016; Metcalfe, 2021). For example, the opening times of the Palaeo-Tethys were estimated ranging from Early–Middle Devonian to Early Carboniferous (Zhong, 1998; Liu et al., 2011b). The Middle to Late Triassic, Early Triassic, Late Permian or Early Palaeozoic has also been proposed as closing times of the ocean (Sengör and Hsü, 1984; Wang and Metcalfe, 2000; Hoa et al., 2008; Nakano et al., 2008, 2010; Jian et al., 2009b; Liu et al., 2012; Zi et al., 2012a, 2012b; Chen et al., 2014; Zhang et al., 2014; Huang and Opdyke, 2016). The question of whether the Ailaoshan–Song Ma Ocean was broad or narrow still obstructed our understanding of the eastern Palaeo-Tethys evolution (Metcalfe, 2002, 2011; Liu et al.,

2011b; Wang et al., 2014; Li et al., 2021; Wang et al., 2021).

Based on structural and provenance analyses of the Ailaoshan–Song Ma ophiolitic mélange matrix, Li et al. (2021) subdivided it into three units: M1, M2, and M3. These units are contacted with each other by faults. Although it is difficult to distinguish them via field observation given that most of them have been deformed and metamorphosed, the distinctive detrital zircons age spectra and $\varepsilon_{Hf}(t)$ values of these unit suggested that they are related to different provenances (Li et al., 2021). As a major part, M1 is located in the middle segment of Ailaoshan–Song Ma ophiolitic mélange, with age peaks at 435 and 970 Ma (Li et al., 2021). M2 is located in the northwestern segment and has a single age peak at 260 Ma (Li et al., 2021). M3 distributes in the southeastern segment of the Ailaoshan–Song Ma ophiolitic mélange, and its main conspicuous age peak is 245 Ma (Li et al., 2021). The distribution model of M1, M2, and M3 along the Ailaoshan–Song Ma ophiolitic mélange shows a significantly heterogeneous pattern that reveals the variations of provenances among different segments of the Ailaoshan–Song Ma Ocean (Li et al., 2021; Lin et al., 2022). The different provenances of these three units also correspond to the different evolutionary stages of the eastern Palaeo-Tethys (Li et al., 2021; Wang et al., 2021).

Our previous work confirmed that the Ailaoshan–Song Ma ophiolitic mélange is heterogeneous in its strike–parallel distribution, which helped to reveal the evolution of the eastern Palaeo-Tethys. However, our understanding of the strike–perpendicular distribution of the units is inadequate due to a lack of detailed and direct evidence,

which further restricts our comprehensive understanding of the evolution of the eastern Palaeo-Tethys.

Therefore, to better understand the spatial heterogeneity of the ophiolitic mélange and its role in the evolution of the eastern Palaeo-Tethys, this study focuses on the areas from the middle to the northwestern segment of the Ailaoshan ophiolitic mélange, which were intensely reworked by the Cenozoic deformation (Fig. 1; Wang et al., 2022), and for which there is a lack of detailed information. Five samples from the matrix of the Ailaoshan ophiolitic mélange were collected for zircon U–Pb dating and Lu–Hf isotope analyses. Using provenance and structural analyses, we can reclassify and reconstruct the geometry of the Ailaoshan ophiolitic mélange, and then discuss the ocean opening and subduction times as well as Cenozoic tectonic superimposition to further enhance our understanding of the evolution of the eastern Palaeo-Tethys.

2 Geological setting

The NW–SE trending Ailaoshan belt extends more than 500 km within southeastern Yunnan Province in southwest China (Fig. 1). Topographically, the belt widens from northwest to southeast owing to tectonic extrusion caused by the collision of the Indian and Eurasian continents during the Cenozoic (Tapponnier et al., 1990) and the Cenozoic strike–slip faults also transformed the tectonic framework.

The Ailaoshan belt can be divided into four tectonic zones based on lithological and structural characteristics: the Western Ailaoshan, Central Ailaoshan, Eastern Ailaoshan and Jinping zones, each of which is described in the following sub-sections (Fig. 1B, Fig. 2; Faure et al., 2016a, 2016b; Li et al., 2021; Wang et al., 2022).

2.1 The Western Ailaoshan zone: a magmatic arc

The Western Ailaoshan zone comprises a sequence of undeformed, unmetamorphosed locally cleavaged Jurassic–Cretaceous sandstone and mudstone which unconformity overlain above Permian-Early Triassic volcanic-volcanoclastic rocks, including basalt–andesite, tuffs, and graywackes. Zircon U–Pb dating of Wusu intermediate and Yaxuanqiao mafic volcanic rocks of this volcanic sequence yield 287–247 Ma (Fig. 2; Fan et al., 2009, 2010; Jian et al., 2009a, 2009b; Liu et al., 2011a; Lai et al., 2014b). This volcanic sequence is conformably underlain by Carboniferous sandstone and mudstone (Fan et al., 2010). Simultaneously, the geochemical data show evidence of both MORB (Mid-Ocean Range Basalt) and arc affinities (Fan et al., 2010; Lai et al., 2014b), and the Western Ailaoshan zone is therefore recognized as a magmatic arc related to the subduction of the Ailaoshan Ocean (Jian et al., 2009a, 2009b; Fan et al., 2010; Lai et al., 2014b; Faure et al., 2016b).

2.2 The Central Ailaoshan zone: an ophiolitic mélange

The Central Ailaoshan zone comprises abundant ultramafic, mafic, granitic, silicious rocks and limestone blocks which are enclosed into the sandy and muddy matrix. Metamorphism of the rocks in this zone was generally low greenschist to low amphibolite facies (Zhong, 1998). Zircons yield U–Pb ages of 383 ± 4, 376 ± 4 and 365 ± 7 Ma for the gabbro, plagiogranite and dolerite, respectively (Jian et al., 2009b; Lai et al., 2014b). The geochemical characteristics of the mafic rocks show an N-MORB-like and suggest that they were formed either in an oceanic or back-arc setting (Xu and Castillo, 2004). Chert with Late Devonian to Early Carboniferous radiolarian indicates a deep-water depositional environment (Mo et al., 1998; Shen et al., 2001).

Based on a thorough examination of the lithological, chronological, geochemical, and palaeontological evidences, the Central Ailaoshan zone is regarded as a dismembered ophiolitic mélange known as the Ailaoshan ophiolitic mélange which could be correlated with the Jinshajiang and Song Ma ophiolitic mélanges to the northwest and southeast, respectively (e.g., Zhong, 1998; Jian et al., 1998, 2009a, 2009b; Yumul et al., 2008; Fan et al., 2010; Faure et al., 2014, 2016a, 2016b; Lai et al., 2014a, 2014b; Li et al., 2021; Wang, 2022; Wang et al., 2022). Radiometric ages and fossils support the opening time of the eastern Palaeo-Tethys during the Late Devonian to Early Carboniferous (Zhong, 1998; Jian et al., 2009a, 2009b).

Moreover, along this zone, the felsic magmatism which is characterized by leucogranite, biotite granite, rhyolite, tuffs, and pyroclastic rocks with 250–240 Ma U–Pb ages is interpreted as the products of crustal melting during syn-collision or post-collision settings (Lai et al., 2014b).

2.3 The Eastern Ailaoshan zone: a Cenozoic tectonite of SCB

The Eastern Ailaoshan zone, namely the Ailaoshan Complex comprises orthogneiss (partly with an augen structure), migmatite, paragneiss, amphibolite, metasandstone, quartzite and marble (Zhong, 1998; Liu et al., 2011b). Metamorphism of the rocks in this zone was generally greenschist to amphibolite facies and even high amphibolite to granulite facies (Zhong, 1998). Zircons from amphibolite and gneiss yield U–Pb ages of 800–850 Ma (Cai et al., 2015) and 750–770 Ma (Qi et al., 2012, 2014), respectively, indicating that the Neoproterozoic magmatic rocks underwent late-stage metamorphism and deformation events (Liu et al., 2011b). Moreover, 230–250 Ma and 20–30 Ma ages are also obtained from plutons or gneiss in this zone (Schärer et al., 1990, 1994; Zhang and Schärer, 1999; Gilley et al., 2003; Sassier et al., 2009; Qi et al., 2010), indicating that this zone was reworked in the Triassic and Cenozoic.

2.4 The Jinping zone: a piece of the ELIP

The Jinping zone comprises an Early Palaeozoic series with Ordovician limestone and mudstone, as well as Silurian–Devonian turbiditic rocks (YNBGMR,

2000). The most significant rock type in the Jinping zone is a km-thick series of Late Permian mafic–ultramafic intrusions and volcanic rocks, including gabbro, basalt, basaltic breccia, pyroclastic rocks, and greywacke (Wang et al., 2007). The metamorphism and deformation of this unit are relatively weak. An Early Triassic carbonate series covers the Palaeozoic rocks. The Jinping zone is considered a component of the Emeishan Large Igneous Province because of its high-Ti and low-Ti alkaline basalts (Xiao et al., 2004; Wang et al., 2007). In addition, based on the Early Permian andesite–basalt–picrite series to Late Permian–Early Triassic komatiite–basalt and trachybasalt–trachyandesite–trachydacite series, the Jinping zone is interpreted as a Permian–Late Triassic rift that extends to the Song Da zone in Vietnam (Liu et al., 2011b). Furthermore, detrital zircons from Silurian sandstone revealed an SCB affinity (Xia et al., 2016) and this zone is also considered to be a part of the Palaeozoic cover of the SCB (Xia et al., 2016).

3 Analytical procedures

Zircons were separated using conventional heavy liquid and magnetic methods before being picked under a binocular microscope. From >500 zircon grains, ~300 was randomly selected and mounted in epoxy resin before being polished to reveal the inner part of the zircon grains. The internal structure of the zircon grains was determined using transmitted and reflected light images as well as cathodoluminescence (CL) images, and these images were captured using a JSM6510 scanning electron microscope equipped with a cathode fluorescence probe device

system.

The zircon U–Pb dating and *in situ* Lu–Hf isotope analyses were performed at the Laboratory of Isotope Geochemistry, Wuhan Centre of China Geological Survey. Zircon U-Pb dating was conducted on a laser ablation inductively coupled plasma mass spectrometry (LA–ICP–MS) equipped with a RESOlution LR/S155 193 nm ARF excimer laser ablation system and an iCAP–Q ICP–MS. The diameter of the laser beam spot was 29 μm and the laser ablation time, frequency, and laser energy density were 45 s, 3 Hz, and 4 J/cm^2, respectively. The international zircon standard 91500 was used as the external standard to calibrate the U–Th–Pb ratios and absolute U abundances. The reference zircon Plešovice was analyzed as an "unknown" to monitor the reproducibility and instrument stability. NIST SRM610 and ^{29}Si were used as the external and internal standards, respectively, to determine the element content. The confidence limit in a single data point was 1σ. More details on operational parameters and analytical methods were reported by Qiu et al. (2021). The original U–Pb isotopic compositions of zircons were obtained using ICPMSDataCal software (version 10.9) (Liu et al., 2008). The zircon age was calculated using the isoplot software (Ludwig, 2003).

The zircon Lu–Hf isotopes were analyzed using a Neptune Plus multi-collector ICP–MS equipped with a RESOlution laser ablation system (LA–MC–ICP–MS). Zircon Lu–Hf isotope analyses points were determined near the LA–ICP–MS age test points. The laser beam diameter, ablation time, frequency, and energy density were 43

μm, 60 s, 6 Hz, and 3 J/cm^2, respectively. Reference zircons Penglai and Plésovice were used as the unknowns to check the reliability of the analytical method. The interference of ^{176}Lu to ^{176}Hf was corrected by ^{176}Lu/^{175}Lu = 0.02656 (Blichert-Toft et al., 1997), and the fractionations of Lu and Hf were assumed to be similar. The interference of ^{176}Yb to ^{176}Hf was corrected by the measured interference-free ^{173}Yb, and the ^{176}Yb/^{173}Yb ratio was set to 0.78696 (Thirlwall and Anczkiewicz, 2004) for calculation. Integration of the analyzed signals and mass bias calibrations was performed using ICPMSDataCal software (version 10.9) (Liu et al., 2008). The operational parameters and analytical methods were described in greater detail by Qiu et al. (2021). The calculation formulas for the $\varepsilon_{Hf}(t)$ and Hf model ages are provided in Supporting Information S2.

4 Results of sample analyses

4.1 Sampling and petrography

Five samples were collected from the matrix of the middle and northwestern segments of the Ailaoshan ophiolitic mélange, from Longjie to Mojiang (Fig. 2, Table 1). The matrix comprises siltstone and sandstone that are intensely deformed (AS391, AS397, AS405, AS420), or intensely cleavaged (AS423), and these are described as follows:

AS391 refers to siltstone as the country rock of the ultramafic rocks. This rock experienced an intense deformation exhibited by schistosity and shear bands (Fig. 4A). In the thin section, the foliation is defined by orientated muscovite and elongated quartz. However, some large quartz grains were fractured along the foliation and recrystallized. The main detrital components are quartz (~50%), muscovite (~45%), and a few feldspars that were mainly altered into kaolinite or sericite. The detrital grain size varies from 0.01 to 0.09 mm with a concentration of ~0.03–0.05 mm (Fig. 5A).

AS397 was sampled in a medium–fine-grained sandstone interbedded with pelite (Fig. 4B). The main detrital components are quartz (~70%) and lithic fragments (~20%), with minor muscovite, sericite, and chlorite. The sample grain sizes range from 0.03 to 0.42 mm with a mean of 0.2–0.3 mm. The sample matrix comprises fine-grained sedimentary particles sandwiched between angular and sub-angular quartz grains. Schistosity presented in this sample is featured by orientated quartz and muscovite under microscope, with a quartz length/width ratio of 3:1 (Fig. 5B).

Similar to AS391, the AS405 sample is also siltstone taken from the host rocks of ultramafic rocks. These rocks recorded intense shearing to form schistosity and quartz boudin. In the thin sections, the schistosity is defined by orientated muscovite and elongated quartz (Fig. 4C). The detrital components consist mainly of quartz (~ 65%) and muscovite (~ 30%) with grain sizes <0.02mm (Fig. 5C).

AS420 is a sheared medium–fine-grained sandstone with a cleavage structure enclosing a lentoid serpentinite block (Fig. 4D). The detrital particles are primarily quartz (~70%) and lithic fragments (~20%), with sizes varying from 0.03 to 0.70 mm and a mean of 0.1–0.3 mm (Figs. 5D and 5E). Muscovite and altered chlorites are distributed in the gaps between quartz grains and parallel to the schistosity.

AS423 is a poorly sorted sandstone with a cleavage structure (Fig. 4E). The detrital components consist of quartz (~65%), lithic fragments, muscovite, and sericite, with grain sizes varying from 0.05 to 0.25 mm and double peaks at 0.05–0.1 and 0.2–0.25 mm (Figs. 5E and 5F).

4.2 Zircon U–Pb dating results

AS391: Most of the zircon grains in this sample are sub-angular to sub-rounded, colorless and transparent while few are prismatic. Their lengths range from 42 to 122 μm with length/width ratios of 1.0–2.4 (Fig. 6, Table S1). A total of 100 zircon grains were selected for dating and rare earth element analyses and 96 concordant ages were obtained. Most zircons have well-defined zonal structures, indicating a magmatic origin. The trace element Th/U ratios of only three grains are <0.1, while those of others range from 0.23 to 1.89, also indicating a magmatic origin. Except for the youngest age of 251 Ma (Table 3), other concordant ages range from 412 to 2772 Ma, with two significant peaks at 435 and 970 Ma and several sub-peaks at 730, 1180,

1360, 1780, and 2400 Ma (Fig. 7A).

AS397: The zircon grains in this sample are colorless and transparent. Morphologically, the grains are sub-angular, rounded to sub-rounded, with lengths of 64–145 μm and length/width ratio of 2.5:1–1:1 (Fig. 6, Table S1). The CL images of most zircons show zonal structures typically of magmatic origin. In addition, 99 of the 100 U–Pb analyzed zircon grains yield concordant ages. The Th/U ratios of most grains are >0.1, suggesting a magmatic origin. The concordant ages range from 355 to 2712 Ma, with two significant peaks at 430 and 960 Ma as well as several sub-peaks at 780, 1145, 1590, 1810, 1970, and 2560 Ma (Fig. 7C).

AS405: Most of the dated zircon grains in this sample are colorless, transparent, sub-rounded to sub-angular, with lengths of 94–165 μm and length/width ratios of 2.4:1–1:1 (Fig. 6, Table S1). All of the analyzed zircons have concordant ages. The internal characteristics of the zircons exhibit zonal structures with Th/U ratios >0.1, indicating a magmatic origin. Similar to AS397, the concordant ages range from 358 to 2808 Ma, with two prominent peaks at 435 and 960 Ma as well as several sub-peaks at 805, 1110, 1380, 1580, 1790, and 2450 Ma (Fig. 7C).

AS420: The zircons in this sample are colorless, transparent, sub-rounded, sub-angular to rounded, with lengths of 69–166 μm and length/width ratios of 2.7:1–1:1 (Fig. 6, Table S1). Most of the zircons have sharp zonal structures that indicate a magmatic origin. All of the analyzed grains yield concordant ages ranging from 395

to 3100 Ma. The age histogram indicates a multimodal distribution with two significant peaks at 435 and 965 Ma and several sub-peaks at 1150, 1450, 1830, and 2480 Ma (Fig. 7D).

AS423: The dated zircon grains are colorless, transparent, sub-angular and sub-rounded to rounded in shape with lengths of 51–125 μm and length/width ratios of 2.7:1–1:1 (Fig. 6, Table S1). A total of 100 grains were analyzed, with 94 grains having concordant ages. Except for four grains, the other Th/U ratios are >0.1, indicating a magmatic origin. The concordant ages range from 414 to 2635 Ma, with one Archean age of 3516 Ma, two significant peaks at 425 and 925 Ma and several sub-peaks at 780, 1120, 1635, 1930, and 2420 Ma (Fig. 7E).

All the LA-ICP-MS U–Pb results of the samples are provided in Supporting Information S1.

4.3 Zircon Lu–Hf isotopic analyses

First, the zircon grains in each sample were grouped based on their age spectrum. Subsequently, 5–7 representative dated grains in each group around the age peak were selected for Lu–Hf isotope analyses. In addition, all the grains with concordant ages in the AS397 sample were analyzed to constrain the statistical significance.

AS391: In this sample, 34 dated grains with ages of 433–2532 Ma were analyzed.

The $\varepsilon_{Hf}(t)$ values for these zircons range from −23.55 to 7.05 (Fig. 8), with a peak at −0.60. The calculated T_{DM}^2 ages vary from 1.11 to 3.27 Ga, with peaks at 1.98, 2.26, 1.58, and 3.18 Ga (Fig. 9A).

AS397: In this sample, 99 zircon grains with ages of 355−2712 Ma were analyzed, with 95 providing valid results. The $\varepsilon_{Hf}(t)$ values range from −25.38 to 11.99 (Fig. 8) with four peaks at −1.80, −9.10, −5.10, and −0.25. The T_{DM}^2 ages vary from 1.0 to 3.96 Ga with peaks at 2.30, 2.01, and 2.83 Ga (Fig. 9B).

AS405: In this sample, 35 dated grains were analyzed, with ages of 409−2547 Ma. The $\varepsilon_{Hf}(t)$ values range from −10.50 to 9.56 (Fig. 8), with a peak at −2.65 and a sub-peak at −8.95. The T_{DM}^2 ages vary from 1.35 to 3.16 Ga, with peaks at 1.98, 2.30, 2.75, 1.38, and 3.15 Ga (Fig. 9C).

AS420: In this sample, 33 dated grains were analyzed, with ages of 434−3100 Ma, with 32 providing valid results. The $\varepsilon_{Hf}(t)$ values range from −23.87 to 6.03 (Fig. 8), with a peak at −0.80 and a sub-peak at −7.50. The T_{DM}^2 ages vary from 1.20 to 3.95 Ga, with peaks at 2.02, 2.84, 1.38, and 3.42 Ga (Fig. 9D).

AS423: In this sample, 35 dated grains were analyzed, with ages of 425−3516 Ma, with 34 providing valid results. The $\varepsilon_{Hf}(t)$ values range from −17.86 to 6.59 (Fig. 8), with two peaks at −4.25 and −8.65 and a sub-peak at −15.25. The T_{DM}^2 ages vary from 1.26 to 3.73 Ga with peaks at 2.06, 2.85, 2.45, 3.21, and 3.69 Ga (Fig. 9E).

All the Lu–Hf results of the samples are provided in Supporting Information S2.

5 Discussion

5.1 Sample classification and units' reconstruction

As mentioned above, we confirmed that the Ailaoshan ophiolitic mélange can be divided into several individual areas based on the different depositional ages and provenances. The strike–parallel heterogeneity is strongly reflected by the M1, M2, and M3 units (Li et al., 2021 and references therein).

The M1 unit is mainly exposed in the middle segment of the Ailaoshan ophiolitic mélange and also in the Song Ma ophiolitic mélange in NE Vietnam (Li et al., 2021). The detrital zircon age spectrum of this unit is characterized by two significant peaks at 435 and 970 Ma (Table 2), with several sub-peaks at 810, 1085, 1690, 1860, and 2510 Ma (Fig. 7F). The $\varepsilon_{Hf}(t)$ values range from −23.30 to 10.32, with an average of −4.76, with 77% of the values being negative (Table 2). In addition, the T_{DM}^{2} ages of zircons show several peaks at Mesoproterozoic to Archean (peaks: 1.55, 2.05, 2.35, and 2.95 Ga; Fig. 9F).

The M2 unit is found cropping out in the northwestern segment of the Ailaoshan ophiolitic mélange (see Fig.2 in Li et al., 2021). The detrital zircon ages are primarily concentrated at 250–280 Ma, with a major age peak at 260 Ma and several sub-peaks

at 410, 770, 950, 1840, and 2480 Ma. The T_{DM}^{2} ages of the 240–280 Ma zircons show a significant Neoproterozoic peak at 0.85 Ga. Meanwhile, the $\varepsilon_{Hf}(t)$ values of the 240–260 Ma zircons range from –1 to 7, indicating a noteworthy mantle contribution.

The M3 unit is mainly located in the southeastern segment of the Ailaoshan and Song Ma ophiolitic mélange (Li et al., 2021). The detrital zircon age spectrum shows a very significant age peak at 245 Ma, with three minor age peaks at 360, 770 and 1045 Ma, respectively. The $\varepsilon_{Hf}(t)$ values of most detrital zircons are negative and concentrated between –17 and –5, and the T_{DM}^{2} ages show two age peaks at 1.3 and 1.8 Ga.

Provenance analysis showed that both the upper and lower plates are potential provenances for the ophiolitic mélange between the SCB and IB (Li et al., 2021; Wang et al., 2021; Lin et al., 2022). Along the suture zone, the components of the mélange present a significant heterogeneity. As previously mentioned, many studies have focused on the southern part of the Ailaoshan ophiolitic mélange and the Thanh Hoa area in the southern part of the Song Ma belt (Xia et al., 2020), while few studies have focused on the northwestern segment.

Due to a lack of detailed work, the M2 unit was determined from the samples of Xia et al. (2020). According to the GPS coordinates, the samples were obtained at a slight distance from the ophiolitic mafic and ultramafic rocks of the ophiolites (Fig. 2). Five samples were collected and analyzed to determine the detailed geometry of the

northwestern segment of the Ailaoshan ophiolitic mélange. AS391, AS397 and AS405 samples were collected from the prolongated part of the M1 unit (Li et al., 2021), while the AS420 and AS423 samples were collected from the interior part of the previously determined M2 unit (Li et al., 2021).

As mentioned in Section 4.2, our five samples share consistent age spectra and similar $\varepsilon_{Hf}(t)$ values and T_{DM}^2 ages (Figs.7, 8, and 9). As inferred from our previous study and field observations, the five samples are highly comparable with the content of the M1 unit (Fig. 7F). Lithologically, all of them are siltstone and sandstone with cleavage, schistosity, or foliation, indicating superimposed deformation (Figs. 4 and 5). The $\varepsilon_{Hf}(t)$ values ranged from –25.38 to 11.99, with an average of –4.06, and 70% are negative in these five samples (Fig. 9). The T_{DM}^2 ages varied from 1.0 to 3.96 Ga, clustering at 2.0, 2.30, 2.82 and 1.40 Ga (Figs. 9 and 10). The Phanerozoic zircons showed $\varepsilon_{Hf}(t)$ values ranging from –25.38 to 6.08 (Fig. 8).

Therefore, it is almost certain that the five samples belong to the M1 unit, even though it was previously believed that the NW segment of the Ailaoshan belt belonged to the M2 unit (Li et al., 2021). Our data, therefore, suggest that the M1 unit extends to the northwest in this region and that both the M1 and M2 units are distributed in the northwestern segment of the Ailaoshan ophiolitic mélange (Fig. 2). The results of this study, therefore, broaden our understanding of the distribution of the M1 unit and update current knowledge about the former spatial distribution of the units (Fig. 2; Table 2).

5.2 Provenance of the detrital zircons in the M1 unit

With the previous five samples from the M1 unit, there would be a total of ten samples (AS103, AS147, TH05, YN41, YN54, AS391, AS397, AS405, AS420 and AS423) of detrital zircon work on the M1 unit. Furthermore, we redefined the composition of the M1 unit. The following information was determined: (1) The detrital age spectrum showed two obvious age peaks at 430 and 960 Ma with secondary peaks at 785, 1160, 1790, 2390, and 2500 Ma. The youngest age cluster was at 355–375 Ma (Fig.7F; Table 3). (2) The $\varepsilon_{Hf}(t)$ values ranged from –25.38 to 11.99 (Table 2), with 72% of the values being negative. (3) The T_{DM}^{2} ages ranged from 0.75 to 3.96 Ga, with several peaks at 2.00, 2.30, 2.83, and 1.40 Ga (Fig. 9F).

Because 400–500 Ma zircon grains are the main age groups, they can help us trace the provenance of the M1 unit (Table 2, Fig. 7F). Because most zircons are of magmatic origin, the detrital grains could be supplied directly from the magmatic rocks or indirectly from the recirculation of sediments. The Early Palaeozoic magmatic events (400–500 Ma) are widespread in the Cathaysia Block (CB) and IB. Hence, we will discuss below whether the 400–500 Ma detrital zircons were supplied directly from the magmatic rocks in the CB/IB or indirectly from the recirculation of the sediments. The Early Palaeozoic magmatic events in the CB were mainly concentrated at 400–500 Ma (Guo et al., 2021), with an obvious age peak at 435 Ma

(Huang and Wang, 2019 and references therein). The age spectrum of the M1 unit is therefore consistent with magmatic events in the CB (Figs. 11A and 11D). The statistical results of the 400–500 Ma magmatic zircons in the CB show $\varepsilon_{Hf}(t)$ values ranging from –19.39 to 2.38, with an average value of –6.11, and a peak at –5.10, with 95% of the values are negative (Chu et al., 2012; Cui et al., 2013; Li et al., 2015; Wang et al., 2011). The $\varepsilon_{Hf}(t)$ values of the 400–500 Ma detrital zircons from the M1 unit range from –19.63 to 10.28, with an average of –4.04 and two peaks at –0.70 and –7.25, and 75% of the values are negative. Therefore, the $\varepsilon_{Hf}(t)$ values of the M1 unit (Fig. 11B) differ from those associated with magmatism in the CB (Fig. 11E). The T_{DM}^2 ages of magmatic zircons in the CB have two peaks at 1.34 and 1.75 Ga (Fig. 11I), and those from the M1 unit have two peaks at 1.45 and 1.88 Ga (Fig. 11C), which also show differences from the magmatism in the CB (Fig. 11F). Therefore, although they have similar age spectra (peak at 430–435 Ma, Figs. 11A and 11D), the $\varepsilon_{Hf}(t)$ values and T_{DM}^2 ages are significantly different.

The Early Palaeozoic magmatism in the IB is mainly distributed in the northern part of the Kontum Massif (the Dai Loc granitic complex) which was geographically located in the southern part of the Truong Son Belt (Jiang et al., 2020; Shang and Chen, 2022). Similar to the CB, the Early Palaeozoic magmatism in the IB was also concentrated at 400–500 Ma, with a significant peak at 420–440 Ma and a sub-peak at 470–485 Ma (Fig. 11G, J). So, it is difficult to distinguish them from the M1 unit based on detrital age spectra. The corresponding $\varepsilon_{Hf}(t)$ value spectrum of the

magmatic zircons from the Truong Son Belt shows two peaks at –1.11 and 2.34 (Fig. 11H): the value of –1.1 is close to the peak of –0.7 in the M1 unit, but the 2.34 was not significant in the M1 unit (Fig. 11H, B). The T_{DM}^2 ages show the same characteristics: one of the peaks of 1.49 Ga from the Truong Son Belt is close to the peak of 1.45 Ga in the M1 unit, but the other peak of 1.27 Ga differs obviously from that of the M1 unit (Fig. 11I, C). The corresponding $\varepsilon_{Hf}(t)$ value spectrum in the Kontum Massif shows a single peak at –8.33 which is close to the peak of –7.25 in the M1 unit (Fig. 11K, B). The T_{DM}^2 ages show the same comparison characteristics (Figs. 11L and 11C): the single peak of 1.95 Ga in the Kontum Massif is close to the peak of 1.88 Ga in the M1 unit. Therefore, the 400–500 Ma detrital zircons in the M1 unit could have been supplied from the mixing of the magmatic rocks in the Truong Son Belt and Kontum Massif.

Considering the recirculation of the sedimentary rocks, related detrital zircon age patterns have also been reported in the Palaeozoic sedimentary rocks in the IB (Wang et al., 2014; Xia et al., 2016; Wang et al., 2016; Fig. 12), in addition to the Yangtze Block and CB. There is an obvious age group at 700–900 Ma with a significant peak at 810–830 Ma in the western and southwestern Yangtze Block, and these are absent in the M1 unit (Fig. 12). A comparison between the M1 unit and the Palaeozoic strata in South Cathaysia shows that although they both share similar age peaks at 430 Ma (450 Ma in South Cathaysia) and 960 Ma, the age peak at 430 Ma is more obvious than the peak at 960 Ma in the M1 unit, while the South Cathaysia shows an opposite

trend (Fig. 12). These suggest that the Palaeozoic sedimentary rocks in the Yangtze Block and South Cathaysia are not the provenances of the M1 unit. The similarity of detrital zircon age patterns in the M1 unit and IB show that the Palaeozoic sedimentary rocks in the IB are the potential sources of the M1 unit (Fig. 12). They share the same age spectrum of zircons with ages between 400 and 500 Ma (Figs. 11A and 11M). The $\varepsilon_{Hf}(t)$ values of zircons (ages at 400–500 Ma) from the Silurian and Devonian sedimentary rocks in the IB range from –15.67 to 13.63, with most (76%) values are negative, and the corresponding T_{DM}^2 ages range from 0.58 to 2.41 Ga (Figs. 11N and 11O). Therefore, the distributions of detrital zircon ages, $\varepsilon_{Hf}(t)$ values, and T_{DM}^2 ages in the M1 unit are in agreement with those of Silurian and Devonian sedimentary rocks in the IB (Fig. 11M and 11A, 11N and B, 11O and C; Xia et al., 2016).

Synthetic comparisons (Fig. 11J and 11M, 11K and 11N, 11L and 11O) show that the $\varepsilon_{Hf}(t)$ values and T_{DM}^2 ages from the magmatic zircons of the Kontum Massif and detrital zircons from the Silurian–Devonian strata in the IB are almost coincident with each other. This suggests that the Kontum Massif offered abundant Early Palaeozic zircons to the Silurian–Devonian strata in the IB. Therefore, there could be another speculation that the 400–500 Ma detrital zircons in the M1 unit could have been supplied from the mixing of detrital zircons from the Silurian–Devonian strata in the IB and magmatic rocks from the Truong Son Belt. Given that most zircons aged 400–500 Ma are broken and sub-rounded suggesting long-time or long-distance

recirculation, we believe this hypothesis is more plausible (Fig. 6 and Table S1).

Therefore, we supposed that the detrital zircons of the M1 unit are primarily supplied from the Silurian–Devonian strata of the IB with the addition of a certain number of magmatic zircons from the Truong Son Belt. A large number of gabbro, diabase, and anorthosite with ages of ~370 Ma have been reported in the Ailaoshan–Song Ma ophiolitic mélange, which was considered to be related to the initial opening of the Palaeo-Tethys Ocean (Jian et al., 2009a; Vuong et al., 2013; Lai et al., 2014a; Zhang et al., 2014, 2020). Based on this assumption, we can speculate that contemporaneous acidic magmatism occurred and that these contemporaneous magmatic rocks are likely the source of the youngest age cluster (355–375 Ma) in the M1 unit.

5.3 The geometry of the Ailaoshan belt with the understanding of the modification of the Cenozoic tectonics

The southwestern boundary between the Central and Western Ailaoshan zones is NE-dipping in the field, which suggests that the Ailaoshan ophiolitic mélange is located upon the schistose Permian or Triassic sedimentary rocks (the sedimentary cover of the IB) (Fig. 2). Similarly, the southwestern boundary between the Eastern and Central Ailaoshan zones is also NE-dipping, which indicates that the Ailaoshan complex is located upon the Ailaoshan ophiolitic mélange (Fig. 2). As the

metamorphism grade increases from the Western to the Eastern Ailaoshan zone, we infer that the Eastern Ailaoshan zone was thrusted upon the Central Ailaoshan zone and that the Central Ailaoshan zone was thrusted upon the Western Ailaoshan zone (Fig. 3). These inverted geometries and SW-ward kinematics are also supported by the other structures, such as the highly sheared quartz schist, SW-ward isoclinal folds and recumbent folds (Wang, 2022; Wang et al., 2022).

Based on the observation of the NE-dipping cleavages in the Late Triassic and Jurassic strata, we interpret the SW-ward deformation as a Cenozoic structure. Since the deformation of the Red River Fault played a dominant role in the Ailaoshan belt in the Cenozoic, we relate the inverted geometry and SW-ward kinematics in the Ailaoshan belt with the activation of the Red River Fault (Fig. 3). In the Cenozoic, the Red River Fault intensely reworked the Ailaoshan Belt, especially the Eastern Ailaoshan zone (Ailaoshan Complex). High-temperature metamorphism (Zhong, 1998), pervasively strike–slip deformation (Zhang and Schärer, 1999; Liu et al., 2011b), and abundant SW-ward isoclinal folds (Fig. 3; Leloup et al., 1995; Wang et al., 2022) there indicate a transpressive deformation of the Red River Fault like a positive-flower structure: the crust-scale strike–slip deformation accompanied with SW-ward thrust on the shallow depth (Fig. 13E).

As mentioned in Section 5.1, the M1 and M2 units coexist in the northwestern segment of the Ailaoshan ophiolitic mélange. Both the M1 and M2 units are NE-dipping, and the M2 unit is located to the southwest of the M1 unit, therefore, the

M2 unit is located under the M1 unit (Fig. 3). In agreement with our previous work, the depositional ages of the M1 and M2 units are considered to be 310-270 and 270-260 Ma, respectively (Li et al., 2021). The present geometry of the M1 and M2 units suggests that the M1 unit was thrusted southwestward upon the M2 unit, indicating a tectonic inversion geometry (Fig. 3). This inverted geometry and SW-ward kinematics are in line with the whole Ailaoshan belt discussed above. Therefore, the transpressive deformation of the Red River Fault gives rise to the inverted geometry and SW-ward kinematics in the whole Ailaoshan belt including the NW segment (Figs. 3 and 13E).

Our previous work showed that the components and provenances of the Ailaoshan–Song Ma ophiolitic mélange are different, indicating a strike–parallel heterogeneity. In this work, the superposition of the M1 and M2 units revealed by the Cenozoic deformation suggests that the Ailaoshan ophiolitic mélange also has a strike–perpendicular heterogeneity.

5.4 Tectonic evolution of the eastern Palaeo-Tethys

It is well acknowledged that since the Middle to Late Devonian, several continental blocks, such as the SCB, IB, Sibumasu, North Qiangtang and South Qiangtang, were separated from Gondwana, drifted to the north and then collided or accreted onto the Laurasia, along with the opening and closing of the Palaeo-Tethys.

In the research area, the Ailaoshan–Song Ma Ocean opened between the SCB and IB as the middle branch of the eastern Palaeo-Tethys. Therefore, in AS397 and AS405 samples, zircons with the youngest age cluster of between 355 and 375 Ma in the M1 unit may have been sourced from the magmatism during this period (Table 3; Fig. 13A).

The Ailaoshan–Song Ma Ocean began to close from the Late Carboniferous to the Early Permian (310-270 Ma) (Li et al., 2021). This closure was accommodated by oceanic subduction under the IB, as shown by the NW–SE striking Western Ailaoshan–Sam Nua–Truong Son magmatic arc belt developed along the northern margin of the IB (Hoa et al., 2008; Lepvrier et al., 2011; Liu et al., 2012; Faure et al., 2014; Shi et al., 2015; Wang et al., 2018a, 2018b). The subducted angle of the slab was gentle during this period, and the magmatic arc is located far from the trench. Therefore, the magmatic arc did not supply materials to the M1 unit (Fig. 13B). However, the Upper Permian sediments (Longtan Formation in Fig. 13B) in the retro-arc basin are located near the magmatic arc, and they contain a significant zircon grain population from this period (Xia et al., 2020; Wang et al., 2021). Therefore, we argue that the Silurian–Devonian cover of the IB (Eastern Simao Block) was the main source of the M1 unit (Fig. 13B).

After a short period (270–265 Ma) of magmatic quiescence (Qian et al., 2016, 2019; Hou et al., 2019), the eruption of ELIP in the southwestern SCB (as the passive margin) provided abundant intermediate-acid zircons (Luo, 2007) for the M2 unit

supported by the $\varepsilon_{Hf}(t)$ values (Fig. 13C; Li et al., 2021). It is worth noting that this quiescent period was interpreted as the tectonic transition from subduction to the initial collision, which reasonably accounts for the changes in the petrogenetic types and magma sources of the associated igneous rocks (Qian et al., 2016, 2019; Hou et al., 2019). Generally, the materials in the matrix were supplied by an active continental margin, and a passive continental margin would only supply materials to the mélange if the ocean was narrow (Barber, 2013; Tate et al., 2015). Therefore, the main provenance of the M2 unit was the ELIP on a passive margin, and this shows that the Ailaoshan–Song Ma Ocean was a narrow ocean rather than a broad one (Li et al., 2021; Lin et al., 2022).

During 260–240 Ma, the well-known Indosinian Orogeny formed at the collisional stage (Faure et al., 2014; Lepvrier et al., 2011; Wang et al., 2022). The second magmatic stage supplied detrital zircons to the M3 unit, as indicated by the $\varepsilon_{Hf}(t)$ values and T_{DM}^2 ages (Fig. 13D$_1$; Li et al., 2021). Accommodated by this south-directed subduction, the M1, M2, and M3 units had been thrusting northeastward over the SCB, corresponding to the top-to-the-NE shearing deformation (Fig. 13D$_2$; Wang et al., 2022). The general metamorphism indicates that the presently exposed mélange developed at a depth of ~10–22 km.

In the Cenozoic, the eastward extrusion of IB caused by a continuous compression produced by the Indian plate into the Eurasian continent was accommodated by the sinistral Red River Fault and featured positive flower structures

(Fig. 13E). In the Ailaoshan ophiolitic mélange, the inverted relationships between the M1 and M2 units are ascribed to the activity of the Red River Fault transpressive deformation.

Conclusions

We conducted a multidisciplinary study including structural analysis, U–Pb dating and Hf determination on matrix detrital zircons in the NW Ailaoshan belt. In association with the results of our previous studies in the same region, the following conclusions can be reached:

(1) The detrital age spectrum of the M1 unit is characterized by two obvious age peaks at 430 and 960 Ma, with several sub-peaks at 785, 1160, 1790, 2390 and 2500 Ma. The provenance of the M1 unit is considered to be mainly related to Silurian–Devonian sedimentary cover of the IB, rather than the SCB or magmatism in South Cathaysia.

(2) Our results imply that the M1 unit extends to the interior of the northwestern segment of the Ailaoshan ophiolitic mélange. From a geometrical perspective, the M1 unit was thrusted upon the M2 unit owing to the Cenozoic transpressive deformation along the Red River Fault.

(3) The spatial relationship between the M1, M2 and M3 units of the ophiolitic mélange indicates not only a strike–parallel but also a strike–perpendicular

heterogeneity of the Ailaoshan suture zone.

Acknowledgments

Prof. Zheng-Xiang Li and two anonymous are acknowledged for their constructive comments and suggestions, which led to a great improvement in our manuscript. This study was funded by the National Natural Science Foundation of China (91855212 and 91855103) and the State Key Laboratory of Lithospheric Evolution, Institute of Geology and Geophysics, Chinese Academy of Sciences (SKL-Z202205). Mr. J.Y. Li is acknowledged for his help during the fieldwork.

References

Barber, A.J., 2013. The origin of mélange: Cautionary tales from Indonesia. J. Asian Earth Sci.76, 428–438.

Blichert–Toft, J, Chauvel, C, Albarède, F., 1997. Separation of Hf and Lu for high–precision isotope analysis of rock samples by magnetic sector–multiple collector ICP–MS. Contrib. Mineral. Petrol. 127(3), 248–260.

Cai, Y.F., Wang, Y.J., Cawood, P.A., Zhang, Y.Z., Zhang, A.M., 2015. Neoproterozoic crustal growth of the Southern Yangtze Block: Geochemical and zircon U–Pb geochronological and Lu–Hf isotopic evidence of Neoproterozoic diorite from the Ailaoshan zone. Precambrian Res. 266, 137–149.

Cawood, P. A., Hawkesworth, C.J., Dhuime, B., 2012. Detrital zircon record and tectonic setting. Geology 40 (10), 875–878.

Chen, Q., Sun, M., Long, X.P, Zhao, G.C, Yuan, C., 2016. U–Pb ages and hf isotopic record of zircons from the late Neoproterozoic and Silurian–Devonian sedimentary rocks of the western Yangtze block: implications for its tectonic evolution and continental affinity. Gondwana Res. 31, 184–199.

Chen, Q., Sun, M., Long, X., Zhao, G.C, Wang, J., Yu, Y., Yuan, C., 2018. Provenance study for the Paleozoic sedimentary rocks from the west Yangtze block: constraint on possible link of South China to the Gondwana supercontinent reconstruction. Precambrian Res. 309, 271–289.

Chen, Z.C., Lin. W., Faure. M., Lepvrier, V., Vuong. N.V., Tich. V.V., 2014. Geochronology and isotope analysis of the Late Paleozoic to Mesozoic granitoids from northeastern Vietnam and implications for the evolution of the South China block. J. Asian Earth Sci. 86, 131–150.

Chu, Y., Lin, W., Faure, M., Wang, Q.C., Ji, W.B., 2012. Phanerozoic tectonothermal events of the Xuefengshan Belt, central South China: Implications from U–Pb age and Lu–Hf determinations of granites. Lithos 150, 243–255.

Chu, Y., Wan, B., Allen, M., Chen, L., Lin, W., Talebian, M., Xin, G.Y., 2021. Detrital zircon age constraints on the evolution of Paleo-Tethys in NE Iran: implications for subduction and collision tectonics. Tectonics 40(8).

Coleman, R.G, 1977. Ophiolites: Ancient Oceanic Lithosphere? Berlin, Springer.

Cui, Y.Y, Zhao, Z.D., Jiang, T., Yang, J.B., Ding, C., Sheng, D., Hou, Q.Y., Hu, Z.C., 2013. Geochronology, geochemistry and petrogenesis of the Early Paleozoic granitoids in southern Jiangxi Province, China. Acta Petrol. Sin. 29 (11), 4011–4024 (in Chinese with English abstract).

Dewey, J.F., 1977. Suture zone complexities: A review. Tectonophysics 40 (1–2), 53–67.

Dewey J.F., 2005. Orogeny can be very short. Proc. Natl. Acad. Sci. U. S. A. 102 (43), 15286–15293.

Dickinson, W.R, Gehrels, G.E., 2009. Use of U–Pb ages of detrital zircons to infer maximum depositional ages of strata: A test against a Colorado Plateau Mesozoic database. Earth Planet. Sci. Lett. 288(1–2), 115–125.

Dilek, Y., Furnes, H., 2011. Ophiolite genesis and global tectonics: Geochemical and tectonic fingerprinting of ancient oceanic lithosphere. Geol. Soc. Am. Bull. 123 (3–4), 387–411.

Dinh, Q.S., 2017. Petrographic characteristics and zircon U–Pb geochronology of granitogneiss rocks in the Chu Lai–Kham Duc area (Quang Nam province). Sci. Technol. Develop. J. Nat. Sci. 1 (6), 258–272 (in Vietnamese with English abstract).

Fan, W.-M., Peng, T.-P., Wang, Y.-J., 2009. Triassic magmatism in the southern Lancangjiang Zone, Southwestern China and its constraints on the tectonic evolution of Paleo-Tethys. Geosci. Front. 16 (6), 291–302.

Fan, W.M., Wang, Y.J., Zhang, A.M., Zhang, F.F., Zhang, Y.Z., 2010. Permian arc-back-arc basin development along the Ailaoshan tectonic zone: Geochemical, isotopic and geochronological evidence from the Mojiang volcanic rocks, Southwest China. Lithos, 119 (3), 553–568.

Faure, M., Lepvrier, C., Vuong, N.V., Tich, V.V., Lin, W., Chen, Z. C., 2014. The South China block–Indochina collision: Where, when, and how? J. Asian Earth Sci. 79, 260–274.

Faure, M., Lin, W., Yang, C., Lepvrier, C., 2016a. Triassic tectonics of the southern margin of the South China Block. C. R. Geosci. 328, 5–14.

Faure, M., Lin W., Chu, Y. Lepvrier, C., 2016b. Triassic tectonics of the Ailaoshan Belt (SW China): Early Triassic collision between the South China and Indochina Blocks, and Middle Triassic intracontinental shearing. Tectonophysics, 683, 27–42.

Fedo, C.M., 2003. Detrital Zircon Analysis of the Sedimentary Record. Rev. Mineral. Geochem. 53(1), 277–303.

Festa, A., Pini, G.A., Dilek, Y., Codegone, G., 2010. Mélanges and mélange–forming processes: a historical overview and new concepts. Int. Geol. Rev. 52, 1040–1105.

Festa, A., Dilek, Y., Pini, G.A., Codegone, G., Ogata, K., 2012. Mechanisms and processes of stratal disruption and mixing in the development of mélanges and broken formations: redefining and classifying mélanges. Tectonophysics 568/569, 7–24.

Gardner, C.J., Graham, I.T., Belousova, E., Booth, G.W., Greig, A., 2017. Evidence for Ordovician subduction-related magmatism in the Truong Son terrane, SE Laos: Implications for Gondwana evolution and porphyry Cu exploration potential in SE Asia. Gondwana Res. 44, 139–156.

Gilley, L.D., Harrison, T.M., Leloup, P.H., Ryerson, F.J., Lovera, O.M., Wang, J.H., 2003. Direct dating of left-lateral deformation along the Red River shear zone, China and Vietnam. J. Geophys. Res.: Solid Earth. 108 (B2), 2127.

Guo, C.L., Liu, Z.K., 2021. Caledonian granites in South China: the geological and geochemical characteristics on their petrogenesis and mineralization. J. Earth Sci. Environ. 43 (6), 927–961 (in Chinese with English abstract).

Harris, R. A., Sawyer, R. K., Audley–Charles, M. G., 1998. Collisional mélange development: Geologic associations of active mélange–forming processes with exhumed mélange facies in western Banda orogen Indonesia. Tectonics, 17, 458–479.

Hess, H. H., 1955. Serpentines, Orogeny, and Epeirogeny, Geol. Soc. Am. Bull. 62, 391–408.

Hoa, T.T., Anh, T.T., Phuong, N.T., Dung, P.T., Anh, T.V., Izokh, A.E., Borisenko, A.S., Lan, C.Y., Chung, S.L., Lo, C.H., 2008. Permo–Triassic intermediate–felsic magmatism of the Truong Son belt, eastern margin of Indochina. C. R. Geosci. 340 (2–3), 112–126.

Hou, L., Xiong, F., Wang, W., Guo, L., Peng, H., Ni, S., Zhang, Q., 2019. Carboniferous-Triassic felsic igneous rocks and typical mineral deposits in the Truong Son orogenic belt, SE Asia: Implications for Paleo-Tethyan tectonic evolution and metallogeny. Ore Geol. Rev. 112, 103036.

Hu, L.S., Du, Y.S., Cawood, P.A., Xu, Y.J., Yu, W.C., Zhu, Y.H., Yang, J.H., 2014. Drivers for late Paleozoic to early Mesozoic orogenesis in South China: constraints from the sedimentary record. Tectonophysics 618, 107–120.

Hu, L.S., Cawood, P.A., Du, Y.S., Xu, Y., J. Xu, W.C, Huang, H., 2015. Detrital records for Upper Permian–Lower Triassic succession in the Shiwandashan Basin, South China and implication for Permo–Triassic (Indosinian) orogeny. J. Asian Earth Sci. 98, 152–166.

Huang, D.-L., Wang, X.-L., 2019. Reviews of geochronology, geochemistry, and geodynamic processes of Ordovician–Devonian granitic rocks in southeast China. J. Asian Earth Sci. 184, 104001.

Huang, K., Opdyke, N. D., 2016. Paleomagnetism of the Upper Triassic rocks from south of the Ailaoshan Suture and the timing of the amalgamation between the South China and the Indochina Blocks, J. Asian Earth Sci. 119, 118–127.

Jian, P., Wang, X.F., He, L.Q., Wang, C.S, 1998. U–Pb zircon dating of the shuanggou ophiolite fromXinping county, Yunnan Province. Acta Petrol. Sin. 12 (2), 207–211 (in Chinese with English abstract).

Jian, P., Liu, D.Y., Kröner, A., Zhang, Q., Wang, Y.Z., Sun, X.M., Zhang, W., 2009a. Devonian to Permian plate tectonic cycle of the Paleo-Tethys Orogen in southwest China (I): Geochemistry of ophiolites, arc/back-arc assemblages and within–plate igneous rocks. Lithos 113 (3–4), 748–766.

Jian, P., Liu, D.Y, Kröner, A., Zhang, Q., Wang, Y., Sun, X.M, Zhang, W., 2009b. Devonian to Permian plate tectonic cycle of the Paleo-Tethys Orogen in southwest China (II): Insights

from zircon ages of ophiolites, arc/back-arc assemblages and within–plate igneous rocks and generation of the Emeishan CFB province. Lithos 113 (3–4), 767–784.

Jiang, W, Yu, J.-H., Wang, X., Griffin, W.L., Pham, T., Nguyen, D., Wang, F., 2020. Early Paleozoic magmatism in northern Kontum Massif, Central Vietnam: Insights into tectonic evolution of the eastern Indochina Block. Lithos 376, 105750.

Lai, C.-K., Meffre, S., Crawford, A.J., Zaw, K., Halpin, J.A., Xue, C.-D., Salam, A., 2014a. The Central Ailaoshan ophiolite and modern analogs. Gondwana Res. 26, 75–88.

Lai, C.-K., Meffre, S., Crawford, A.J., Zaw, K., Xue, C.-D., Halpin, J.A., 2014b. The Western Ailaoshan Volcanic Belts and their SE Asia connection: a new tectonic model for the Eastern Indochina Block. Gondwana Res. 26, 52–74.

Leloup, P.H., Lacassin, R.L, Tapponnier, P., Schärer, U., Zhong, D.L, Liu, X.H, Zhang, L.S, Ji, S.C, Phan, T.T., 1995. The Ailaoshan- Red River shear zone (Yunnan, China), Tertiary transform boundary of Indochina. Tectonophysics 251(1–4), 3–84.

Lepvrier, C., Maluski, H., Van Vuong, N., Roques, D., Axente, V., Rangin, C., 1997. Indosinian NW-trending shear zones within the Truong Son belt (Vietnam): ^{40}Ar-^{39}Ar Triassic ages and Cretaceous to Cenozoic overprints. Tectonophysics 283, 105–127.

Lepvrier, C., Faure, M., Vuong, V.N., Tich, V.V., Lin, W., Thang, T.T., Hoa, P.T., 2011. North-directed Triassic nappes in Northeastern Vietnam (East Bac Bo). J. Asian Earth Sci. 41(1): 56-68.

Li, Q.L., Lin, W., Wang, Y., Faure, M., Meng, L.T., Wang, H., Nguyen, V. V., Hoai, L. T.T., Lepvrier, C., Chu, Y., Wei, W., Vu, T.V., 2021. Detrital zircon U–Pb age distributions and Hf isotopic constraints of the Ailaoshan–Song Ma Suture Zone and their paleogeographic implications for the Eastern Paleo-Tethys evolution. Earth–Sci. Rev. 221.

Li, W., Bi, S.J., Yang, Z., Liang, P., Tang, K.F., 2015. Zircon U–Pb Age and Hf Isotope Characterization of Sheshan Granodiorite in Southern Edge of Dayaoshan, Guidong:

Constraints on Caledonian Diagenesis and Mineralization. Earth Sci. 40 (1), 17–33 (in Chinese with English abstract).

Lin, W., Wang, Q.C, Chen, K., 2008. Phanerozoic tectonics of South China Block: New insights from the polyphase deformation in the Yunkai Massif. Tectonics 27, TC6004.

Lin, W., Rossi, P., Faure, M., Li, X.-H., Ji, W.B., Chu, Y., 2018. Detrital zircon age patterns from turbidites of the Balagne and Piedmont nappes of Alpine Corsica (France): evidence for an European margin source. Tectonophysics 722, 69–105.

Lin, W., Wang, Y., Liu, F., Meng, L.T., Ji, W.B., Wei, W, Chu, Y , So g, C, Wu, Q.Y., 2022. Matrix of the ophiolitic mélange zone and its tectonic im licat ons: Insights of the eastern Paleo-Tethys. Acta Geol. Sin. 96 (10), 3449–3467 (i . Chi ese with English abstract).

Liu, C., Deng, J.F., Liu, J.L., Shi, Y.L., 2011a. Cha a teristics of volcanic rocks from Late Permian to Early Triassic in Ailaoshan tecto o–magmatic belt and implications for tectonic settings. Acta Petrol. Sin. 27 (12), 3590 3602 (in Chinese with English abstract).

Liu, J.L., Tang, Y., Song, Z.J., Tran, M.D., Zhai, Y.F., Wu, W.B., Chen, W., 2011b. The Ailaoshan belt in western Yunnan: tectonic framework and tectonic evolution. J. Jilin Univ., Earth Sci. Ed. 41 (5), 1285–1303 (in Chinese with English abstract).

Liu, J.L, Tran, M.-D., Tang, Y., Nguyen, Q.-L., Tran, T.H., Wu, W.B., Chen, J.F., Zhang, Z.C., Zhao, Z.D., 2012. Permo–Triassic granitoids in the northern part of the Truong Son belt, NW Vietnam: geochronology, geochemistry, and tectonic implications. Gondwana Res. 22, 628–644.

Liu, Y.S., Zong, K.Q., Kelemen, P.B., Gao, S., 2008. Geochemistry and magmatic history of eclogites and ultramafic rocks from the Chinese continental scientific drill hole: Subduction and ultrahigh-pressure metamorphism of lower crustal cumulates. Chem. Geol. 247 (1–2), 133–153.

Ludwig, K R., 2003. ISOPLOT 3.0: A geochronological toolkit for Microsoft Excel (Berkeley Geochronology Center, Berkeley, California). Berkeley, Berkeley Geochronology Center Special Publishing.

Luo, Z.Y., 2007. Chronological and geochemical characteristics of intermediate-acid intrusive rocks in the Emeishan Igneous Province: genetic relationship with the Emeishan Mantle Plume. Guangzhou, Guangzhou Institute of Geochemistry, Chinese Academy of Sciences.

Metcalfe, I., 2002. Permian tectonic framework and Palaeogeography of SE Asia. J. Asian Earth Sci. 20 (6), 551–566.

Metcalfe, I., 2011. Palaeozoic–Mesozoic history of SE Asia. Geol. Soc. Spec. Publ. 355 (1), 7–35.

Metcalfe, I., 2021. Multiple Tethyan Ocean basins and orogenic belts in Asia. J. Asian Earth Sci. 100, 87-130.

Mo, X.X., Shen, S.Y., Zhu, Q.W., Xu, T.R., Wei, Q.R., Tan, J., Zhang, S.Q., Cheng, H.L., 1998. Volcanic rocks–ophiolites and metallogeny in the southern segment of the Three–River area. Beijing, Geological Publishing House (in Chinese).

Mukasa, S.B., Ludden, J.N., 1987. Uranium-lead isotopic ages of plagiogranites from the Troodos ophiolite, Cyprus, and their tectonic significance. Geology 15(9), 825-828.

Nagy, E.A., Maluski, H., Lepvrier, C., Schärer, U., Thi, P.T., Leyreloup, A., Tich, V.V., 2001. Geodynamic significance of the Kontum massif in Central Vietnam: composite $^{40}Ar/^{39}Ar$ and U–Pb ages from Paleozoic to Triassic. J. Geol. 109, 755–770.

Nakano, N., Osanai, Y., Minh, N.T., Miyamoto, T., Hayasaka, Y., Owada M., 2008. Discovery of high-pressure granulite-facies metamorphism in northern Vietnam: Constraints on the Permo-Triassic Indochinese continental collision tectonics. C. R. Geosci. 340(2–3), 127–138.

Nakano, N., Osanai, Y., Sajeev, K., Hayasaka, Y., Miyamoto, T., Minh, N.T., Owada, M., Windley, B., 2010. Triassic eclogite from northern Vietnam: inferences and geological significance. J. Metamorph. Geol. 28(1), 59–76.

Pham, T.H., Nguyen, T.D., Nguyen, T.B.T., Nguyen, T.M., Pham, M., 2016. U–Pb ages and Hf isotopic composition of zircon and bulk rock geochemistry of the Dai Loc granitoid complex in Kontum massif: implications for early Paleozoic crustal evolution in Central Vietnam. J. Mineral. Petrol. Sci. 111, 1–16.

Qi, X.X, Zhu, L.H., Li, H.Q., Hu, Z.C., Li, Z.Q., 2010. Zircon LA-ICP-MS U–Pb Dating for Mylonitized Granite from the Ailaoshan–Jinshajiang Tectonic Zone in the Eastern Qinghai Tibet Plateau and Its Tectonic Significance. Acta Geol. Sin. 84 (3), 357–369 (in Chinese with English abstract).

Qi, X.X., Zeng, L.S., Zhu, L.H., Hu, Z.C., Hou, K.J., 2012. Zircon U–Pb and Lu–Hf isotopic systematics of the Daping plutonic rocks: implications for the Neoproterozoic tectonic evolution of the northeastern margin of the Indochina block, Southwest China. Gondwana Res. 21, 180–193.

Qi, X.X., Santosh, M., Zhu, L.H., Zhao, Y.H., Hu, Z.C., Zhang, C., Ji, F.B., 2014. Mid-Neoproterozoic arc magmatism in the northeastern margin of the Indochina Block, SW China: geochronological and petrogenetic constraints and implications for Gondwana assembly. Precambrian Res. 245, 207–224.

Qian, X., Feng, Q.L., Wang, Y.J., Chonglakmani, C., Monjai, D., 2016. Geochronological and geochemical constraints on the mafic rocks along the Luang Prabang zone: carboniferous back-arc setting in northwest Laos. Lithos 245, 60–75.

Qian, X., Wang, Y., Zhang, Y., Zhang, Y., Senebouttalath, V., Zhang, A., He, H., 2019. Petrogenesis of the Permian–Triassic felsic igneous rocks along the Truong Son zone in northern Laos and their Paleotethyan assembly. Lithos 328–329, 101–114.

Qiu, X.F., Tong, X.R., Jiang, T., Khattak, N.U., 2021. Reworking of Hadean continental crust in the Dabie orogen: evidence from the Muzidian granitic gneisses. Gondwana Res. 89, 119–130.

Rossignol, C., Bourquin, S., Hallot, E., Poujol, M., Dabard, M.P., Martini, R., Villeneuve, M., Cornee, J.J., Brayard, A., Roger, F., 2018. The Indosinian orogeny: a perspective from sedimentary archives of North Vietnam. J. Asian Earth Sci. 158, 352–380.

Sassier, C., Leloup, P.H., Rubatto, D., Galland, O., Yue, Y., Lin, D., 2009. Direct measurement of strain rates in ductile shear zones: A new method based on syntectonic dikes. J. Geophys. Res.: Solid Earth 114, B01406.

Schärer, U., Tapponnier, P., Lacassin, R., Leloup, P.H., Zhong, D.L., Ji, S.C., 1990. Intraplate tectonics in Asia: a precise age for large–scale Miocene movement along the Ailao Shan–Red River shear zone. China. Earth Planet. Sci. Lett. 97 (1): 65–77.

Schärer, U., Zhang, L.-S., Tapponnier, P., 1994. Duration of strike–slip movements in large shear zones: The Red River belt, China. Earth Planet. Sci. Lett. 379–397.

Şengör, A.M.C., 1992. The Paleo-Tethys suture: a line of demarcation between two fundamentally different architectural style in the structure of Asia. Isl. Arc 1 (1), 78–91.

Sengör, A.M.C., Hsü, K., 1984. The Cimmerides of eastern Asia: history of the eastern end of Paleo-Tethys. Mem. Soc. Geol. France, 147, 139–167.

Shang, Z., Chen, Y., 2022. Petrogenesis and Tectonic Implications of Early Paleozoic Magmatism in Awen Gold District, South Section of the Truong Son Orogenic Belt, Laos. Minerals 12(8), 923.

Shao, T.B., Cheng, N.F., Song, M.J., 2016. Provenance and tectonic–paleogeographic evolution: Constraints from detrital zircon U–Pb ages of Late Triassic–Early Jurassic deposits in the northern Sichuan basin, central China. J. Asian Earth Sci. 127, 12–31.

Shen, S.Y., Wei, Q.R., Chen, H.L., Mo, X.X., 2001. Characteristics and geotectonic implications of two sorts of silicalites in Ailao Mountain belt, "Three_River Area", 01, 42–46 (in Chinese with English abstract).

Shi, M. F., Lin, F.-C., Fan, W. Y., Deng, Q., Cong, F., Tran, M.D., Zhu, H.-P., Wang, H., 2015. Zircon U–Pb ages and geochemistry of granitoids in the Truong Son terrane, Vietnam: Tectonic and metallogenic implications. J. Asian Earth Sci. 101, 101–120.

Sinh, V.B.T., Osanai, Y., Nakano, N., Kitano, I., Adachi, T., Tuan, A.T., Pham, B., 2022. Petrology and zircon U–Pb geochronology of pelitic gneisses and granitoids from the Dai Loc Complex in the Truong Son Belt, Vietnam: Implication for the Silurian magmatic-metamorphic event. J. Asian Earth Sci. 226, 105070.

Smith, A. B., Colchen, M., 1988. Late Palaeozoic biogeography of East Asia and palaeontological constraints on plate tectonic reconstructions [and discussion]. Philos. Trans. R. Soc., A. 326 (1589), 189–227.

Tapponnier, P., Lacassin, R., Leloup, P.H., Schärer, U., Zhong, D.L., Wu, H.W., Liu, X.H., Ji, S.C., Zhang, L.S., Zhong, J.Y., 1990. The Ailao Shan–Red River metamorphic belt: Tertiary left-lateral shear between Indochina and South China. Nature, 343 (6257), 431–437.

Tate, G.W., McQuarrie, N., van Hinsbergen, D.J.J., Bakker, R.R., Harris, R., Jiang, H.S., 2015. Australia going down under: Quantifying continental subduction during arc-continent accretion in Timor-Leste. Geosphere 11(6), 1860-1883.

Thirlwall, M. F., Anczkiewicz, R., 2004. Multidynamic isotope ratio analysis using MC–ICP–MS and the causes of secular drift in Hf, Nd and Pb isotope ratios. Int. J. Mass Spectrom. 235 (1), 59–81.

Vuong, N.V., Hansen, B.T., Wemmer, K., Lepvrier, C., Tích, V.V., Thắng, T.T., 2013. U/Pb and Sm/Nd dating on ophiolitic rocks of the Song Ma suture zone (northern Vietnam): Evidence for upper Paleozoic Paleotethyan lithospheric remnants. J. Geodynamics 69, 140–147.

Wang, C., Liang, X., Foster, D.A., Fu, J., Jiang, Y., Dong, C., Zhou, Y., Wen, S., Quynh, P. V., 2016. Detrital zircon U–Pb geochronology, Lu–Hf isotopes and REE geochemistry constraints on the provenance and tectonic setting of Indochina Block in the Paleozoic. Tectonophysics 677–678, 125–134.

Wang, C.Y., Zhou, M.-F., Qi, L., 2007. Permian flood basalts and mafic intrusions in the Jinping (SW China)–Song Da (northern Vietnam) district: mantle sources, crustal contamination and sulfide segregation. Chem. Geol. 243, 317–343.

Wang, Q.F., Deng, J., Li, C.S., Li, G.J., Yu, L., Qiao, L., 2014. The boundary between the Simao and Yangtze blocks and their locations in Gondwana and Rodinia: constraints from detrital and inherited zircons. Gondwana Res. 26 (2), 438–448.

Wang, X.-y., Cao, D.-h., Wang, Z.-q., Wang, A.-j., Wu, Y.-d., 2018a. Zircon U–Pb age, trace element and Hf isotope composition of Sepon Au–Cu deposit, Laos: tectonic and metallogenic implications. China Geol. 1, 36–48.

Wang, X., Metcalfe, I., 2000. The Jinshajiang–Ailaoshan Suture Zone, China: tectonostratigraphy, age and evolution, J. Asian Earth Sci. 18(6), 675–690.

Wang, Y., Lin, W., Faure, M., Lepvrier, C., Chu, Y., Nguyen, V.V., Hoai, L. T.T., Wei, W., Liu, F., Van, T.V., 2021. Detrital zircon U–Pb age distribution and Hf isotopic constraints from the terrigenous sediments of the Song Chay Suture Zone (NE Vietnam) and their paleogeographic implications on the Eastern Paleo-Tethys evolution. Tectonics 40, e2020TC006611.

Wang, Y., 2022. Mesozoic crustal evolution of Jiaobei area and its implications for destruction of the North China Craton. Doctoral thesis. Beijing, Institute of Geology and Geophysics, Chinese Academy of Sciences.

Wang, Y., Lin, W., Faure, M., Nguyen, V.V., Meng, L.T, Chu, Y., Wei, W., Hoai, L.T.T., Lepvrier, C., Van, T.V., Li, Q.L., Wang, H., Chen, Z.C., Wu, L., Wang, F., 2022. Correlation

of the Ailaoshan–Song Ma–Song Chay orogenic belts and implications for the evolution of eastern Paleo-Tethys Ocean. Tectonophysics 843, 229618.

Wang, Y.J., Zhang, A.M., Fan, W.–M., Zhao, G.C., Zhang, G.W., Zhang, Y.Z., Zhang, F.F., Li, S.Z., 2011. Kwangsian crustal anatexis within the eastern South China Block: geochemical, zircon U–Pb geochronological and Hf isotopic fingerprints from the gneissoid granites of Wugong and Wuyi–Yunkai Domains. Lithos 127 (1–2), 239–260.

Wang, Y.J, Qian, X., Cawood, P.A., Liu, H.C, Feng, Q.L, Zhao, G.C., Zhang, Y.H, He, H.Y, Zhang, P.Z, 2018b. Closure of the East Paleotethyan Ocean and amalgamation of the Eastern Cimmerian and Southeast Asia continental fragments. Earth Sci. Rev. 186, 195–230.

Xia, X.P, Nie, X.S, Lai, C.-K., Wang, Y.J, Long, X.P, Moffre, C., 2016. Where was the Ailaoshan Ocean and when did it open: A perspective based on detrital zircon U–Pb age and Hf isotope evidence. Gondwana Res. 36, 488–502.

Xia, X.P., Xu, J., Huang, C., Long, X.P, Zhou, M.L., 2020. Subduction polarity of the Ailaoshan Ocean (eastern Paleotethys): Constraints from detrital zircon U–Pb and Hf–O isotopes for the Longtan Formation. Geol. Soc. Am. Bull. 132, 987–996.

Xiao, L., Xu, Y.G., Mei, H.J., Zheng, Y.F., He, B., Pirajno, F., 2004. Distinct mantle sources of low-Ti and high-Ti basalts from the western Emeishan large igneous province, SW China: implications for plume-lithosphere interaction. Earth Planet. Sci. Lett. 228, 525–546.

Xu, J.-F., Castillo. P.R., 2004. Geochemical and Nd–Pb isotopic characteristics of the Tethyan asthenosphere: implications for the origin of the Indian Ocean mantle domain. Tectonophysics 393 (1), 9–27.

Xu, J., Xia, X.P., Lai, C., Long, X.P., Huang, C., 2019. When did the Paleotethys Ailaoshan Ocean close: New insights from detrital zircon U–Pb age and Hf isotopes. Tectonics 38, 1798–1823.

Xu, Y.J., Du. Y.S., Cawood, P.A., Hu, L.S., 2017.Aulacogen Formation in Response to Opening

the Ailaoshan Ocean: Origin of the Qin–Fang Trough, South China. J. Geol. 125 (5), 531–550.

Yang, L, Wang, Q.F., Wang, Y.N., Li, G.J., 2018. Proto-to Paleo-Tethyan evolution of the eastern margin of Simao block. Gondwana Res. 62, 61–74.

Yumul, G.P., Zhou, M.-F., Wang, Y.C., Zhao, T.-P., Dimalanta, C.B., 2008. Geology and geochemistry of the Shuanggou ophiolite (Ailao Shan ophiolitic belt), Yunnan province, SW China: evidence for a slow–spreading oceanic basin origin. J. Asian Earth Sci. 32, 385–395.

YNBGMR (Yunnan Bureau of Geology and Mineral Resources), 2009. Regional Geology of Yunnan Province. Geological Publishing House, Beijing (in Chinese).

Zhang, L.-S., Schärer, U., 1999. Age and origin of magmatism along the Cenozoic Red River shear belt. China. Contrib. Mineral. Petrol. 134, 67–85.

Zhang, R.Y., Lo, C.-H., Li, X.-H., Chung, S.-L., Anh, T.T., Tri, T.V., 2014. U–Pb dating and tectonic implication of ophiolite and metabasite from the Song Ma suture zone, Northern Vietnam. Am. J. Sci. 314, 649–672.

Zhang, X.C., Wang, Y.J, Clift, P.D., Yan, Y., Zhang, Y.Z, Zhang, L., 2018. Paleozoic tectonic setting and paleogeographic evolution of the Qin–Fang Region, Southern South China Block: detrital Zircon U–Pb geochronological and Hf Isotopic constraints. Geochem. Geophys. Geosyst. 19 (10), 3962–3979.

Zhang, Y.Z., Yang, X., Wang, Y., Qian, X., Wang, Y.J., Gou, Q.Y., Senebouttalath, V., Zhang, A.M., 2020. Rifting and subduction records of the Paleo-Tethys in North Laos: Constraints from Late Paleozoic mafic and plagiogranitic magmatism along the Song Ma tectonic zone. Geol. Soc. Am. Bull. 133, 212–232.

Zhong, D. L., 1998. The Tethyan Orogenic belt in western Yunnan. Beijing, Science Publishing House (in Chinese).

Zhong, N., Song, X.S, Xu, H.Y, Jiang, H.C., 2017. Influence of a tectonically active mountain belt on its foreland basin: Evidence from detrital zircon dating of bedrocks and sediments from the eastern Tibetan Plateau and Sichuan Basin, SW China. Journal of Asian Earth Sciences, 146, 251–264.

Zhu, M., 2016. The depositional record of southwestern Upper Yangtze area during Triassic and its restriction on the tectonic framework of basin and range. Doctor thesis. Zhejiang, Zhejiang University (in Chinese with English abstract).

Zi, J.-W, Cawood, P., Fan, W.-M, Wang, Y.-J, Tohver, E., 2012a. Generation of Early Indochina enriched mantle-derived granitoid pluton in the Sanjiang Orogen (SW China) in response to closure of the Paleo-Tethys. Lithos 140–141, 166–182.

Zi, J.-W., Cawood, P.A., Fan, W.-M., Wang, Y.-J., Tohver, E., McCuaig, T.C., Peng, T.P., 2012b. Triassic collision in the Paleo-Tethys Ocean constrained by volcanic activity in SW China. Lithos 144–145, 145–160.

Figure caption

Fig. 1. (A) Tectonic outline of east Asia (adapted from Lin et al., 2008). (B) Tectonic map of Southwest China-North Vietnam region (adapted from Faure et al., 2014; Li et al., 2021). ALMZ: Ailaoshan ophiolitic mélange zone; WALZ: western Ailaoshan zone; SC: Song Chay massif; SCF: Song Chay Fault; JP: Jinping zone; RRF: Red River Fault; DBF: Dien Bien Phu Fault; SCMZ: Song Chay ophiolitic mélange zone; SMMZ: Song Ma ophiolitic mélange zone; SD: Song Da rift.

Fig. 2. Geological map of the Ailaoshan Belt and adjacent areas with the sample locations (adapted from Li et al., 2021; Wang et al., 2022).

Fig. 3. Cross sections of the Ailaoshan Belt showing the tectonic succession, from the SW to the NE (the location is shown in Fig. 2). ALF: Ailaoshan Fault; RRF: Red River Fault.

Fig. 4. Representative field photos of the outcrop of the sampling location. (A) Intensely sheared siltstone (AS391) as the country rocks of ultramafic rocks. (B) Intensely sheared sandstone in the country rocks of ultramafic rocks (AS397). (C) Intensely sheared siltstone (AS405) with abundant lentoid quartz veins. (D) Intensely cleaved sandstone (AS420) and enclosed lentoid serpentinite. (E) Sandstone with pervasive cleavages (AS423).

Fig. 5. Microphotographs of the analyzed samples. (A) Intensely fractured and recrystallized quartz, feldspar, and oriented mica in AS391 (cross-polarized light). (B) Fractured and recrystallized quartz, feldspar, and oriented mica in AS397 (cross-polarized light). (C) Intensely sheared minerals and abundant sericite in AS405 (cross-polarized light). (D) Sheared and fractured quartz, feldspar in AS420 (cross-polarized light). (E) Sheared and fractured quartz, feldspar in AS420 (plane-polarized light). (F) Fractured quartz and feldspar in AS423 (cross-polarized light).

Fig. 6. Representative cathodoluminescence (CL) images of the analyzed zircons.

Fig. 7. (A–E) Kernel Density Estimate diagrams of the detrital zircon U–Pb ages in this work. (F) Kernel Density Estimate diagrams of the detrital zircon U–Pb ages in this work and the previous M1 unit. Data in the previous M1 unit are from Li et al., 2021 and Xia et al., 2016.

Fig. 8. (A) Temporal variations of $\varepsilon_{Hf}(t)$ values for all detrital zircons in this work and previous M1 unit. (B) Temporal variations of $\varepsilon_{Hf}(t)$ values of detrital zircons with ages <1200 Ma. Data in the previous M1 unit are from Li et al., 2021. DM: Depleted Mantle, LC: Lower Crust.

Fig. 9. (A–E) Kernel Density Estimate diagrams of zircon T_{DM}^{2} ages in this work. (F) Kernel Density Estimate diagrams of zircon T_{DM}^{2} ages in this work and previous M1 unit. Data in previous M1 unit are from Li et al., 2021.

Fig. 10. Diagram of the T_{DM}^2 ages versus age plots for detrital zircons in this work and previous M1 unit, respectively. Kernel Density Estimate diagrams of T_{DM}^2 ages in this work and previous M1 unit. Data in previous M1 unit are from Li et al., 2021.

Fig. 11. Age, εHf(t), and T_{DM}^2 ages spectrum of detrital zircons (400–500 Ma) in the M1 unit (A, B, C), magmatic zircons in the Cathaysia Block (D, E, F), magmatic zircons in the Truong Son Belt (G, H, I), magmatic zircons in the Kontum Massif (J, K, L) and Silurian-Devonian strata in the Indochina Block (M, N, O). Data in the M1 unit are from this work, Xia et al., 2016; Li et al., 2021. Data in the Cathaysia Block are from Chu et al., 2012; Cui et al., 2013; Wang et al., 2011; Li et al., 2015. Data in the Truong Son Belt are from Shi et al., 2015; Pham et al., 2016; Jiang et al., 2020; Shang and Chen, 2022; Sinh et al., 2022. Data in the Kontum Massif are from Nagy et al., 2001; Dinh 2017; Gardner et al., 2017; Jiang et al., 2020. Data in the Indochina Block are from Xia et al., 2016; Yang et al., 2018; Li et al., 2021.

Fig. 12. Synthesis and comparison of Kernel Density Estimate diagrams of detrital zircon ages. Cathaysia Block including the region of Shiwandashan (Hu et al., 2014, 2015) and Qin-Fang area (Xu et al., 2017; Zhang et al., 2018); S. Songpan-Ganzi (W. Yangtze Block) (Chen et al., 2016, 2018; Shao et al., 2016; Zhu, 2016; Zhong et al., 2017); E. Ailaoshan belt (SW. Yangtze Block) (Xia et al., 2016, 2020; Xu et al., 2019); Simao (N. Indochina Block) (Xia et al., 2016, 2020; Yang et al., 2018; Xu et al., 2019); Truong Son belt (Indochina Block) (Wang et al., 2016; Rossignol et al., 2018).

Fig. 13. Schematic reconstruction of the geodynamic evolution between the SCB and IB from Late Devonian to Cenozoic.

Fei Liu: Investigation, Formal analysis, Data curation, Writing - original draft, Writing - review & editing, Visualization.

Wei Lin: Conceptualization, Supervision, Methodology, Investigation, Data curation, Funding acquisition, Writing - review & editing.

Yin Wang: Investigation, Formal analysis, Data curation, Writing - review & editing, Visualization.

Lingtong Meng: Formal analysis, Data curation, Writing - review & editing, Visualization.

Michel Faure: Conceptualization, Supervision, Methodology, Investigation, Data curation, & Review

Vuong Van Nguyen: Review & editing.

Qinying Wu: Investigation.

Yang Chu: Review & editing.

Wei Wei: Methodology, Data curation.

Hoai Luong Thi Thu: Review

Tich Van Vu: Review

Qiuli Li: Methodology, Investigation, Review.

Hao Wang: Methodology, Review.

Ke Chen: Review & editing.

No conflict of interest exits in the submission of this manuscript. All the authors listed have approved the manuscript that is enclosed. Neither the entire paper nor any part of its content has been published or has been accepted elsewhere. It is not being submitted to any other journal at the same time.

Table 1 Summary of the petrography and tectonic locations of the analyzed samples

Samples number	GPS location	Petrography	Tectonic position	Unit	Depositional age
AS391	101.360218° E 23.977939° N	Sheared siltstone	Middle segment of the Ailaoshan ophiolitic mélange	M1	310-270 Ma
AS397	101.421897° E 23.952558° N	Medium-fine grained sandstone			
AS405	101.569676° E 23.734362° N	Schistozed siltstone			
AS420	100.854106° E 24.613683° N	Medium-fine grained sandstone with cleavages	NW segment of the Ailaoshan ophiolitic mélange	Revised from original M2 to M1 unit	310-270 Ma
AS423	100.899897° E 24.592241° N	Sandstone			

Table 2 Summary of the results of U-Pb and $\varepsilon_{Hf}(t)$ values of the analyzed samples in this work and previous M1 unit.

Samples	U-Pb ages	$\varepsilon_{Hf}(t)$ values
AS391	Two major age groups occur at 400–500, and 900–1100, with two significant peaks at 435 and 970 Ma (Figure 7A, Table S1)	-23.55 to 7.05 with a peak at -0.60 (Table S2)
AS397	Two major age groups occur at 350–500, and 850–1050, with two significant peaks at 430 and 960 Ma (Figure 7B, Table S1)	-25.38 to 11.99 with four peaks at -1.80, -9.10, -5.10, and -0.25 (Table S2)
AS405	Two major age groups occur at 350–500, and 850–1050, with two significant peaks at 435 and 960 Ma (Figure 7C, Table S1)	-10.[illegible] to 9.56 with a peak at -2.65 and a [illegible]b-peak at -8.95 (Table S2)
AS420	Two major age groups occur at 390–500, and 850–1050 Ma, with two significant peaks at 435 and 965 Ma (Figure 7D, Table S1)	-23.87 to 6.03 with a peak at -0.80 and a sub-peak at -7.50 (Table S2)
AS423	Two major age groups occur at 410–460, 850–1000 Ma, and a minor age group at 750–800 Ma, with two significant peaks at 425 and 925 Ma (Figure 7E, Table S1)	-17.86 to 6.59 with two peaks at -4.25 and -8.65, and a sub-peak at -15.25 (Table S2)
This work	Two major age groups occur at 400–500, 850–1050 Ma, and a minor age group at 750–850 Ma, with two significant peaks at 430 and 960 Ma (Figure 7F, Table S1)	-25.38 to 11.99 with a peak at -0.95 and a sub-peak at -8.80 (Table S2)
Previous M1 unit	Two major age groups occur at 400–500, 850–1050 Ma, and a minor age group at 750–850 Ma, with two significant peaks at 435 and 970 Ma (Figure 7F, Li et al., 2021 Table S1)	-23.30 to 10.32 with a peak at -3.55 and three sub-peaks at -9.75, -6.9, and +0.20 (Li et al., 2021 Table S2)
This work +Previous M1 unit	Two major age groups occur at 400–500, 850–1050 Ma, and a minor age group at 750–850 Ma, with two significant peaks at 430 and 960 Ma (Figure 7F, Table S1, Li et al., 2021 Table S1)	-25.38 to 11.99 with two peaks at -2.65 and 0, and a sub-peak at -9.15 (Table S2, Li et al., 2021 Table S2)

This work: AS391 + AS397 + AS405+ AS420+ AS423; Previous work: AS103 + AS147 + TH05 + YN41 + YN54 (Xia et al., 2016; Li et al., 2021).

Table 3 Summary of the four measures of the youngest age of detrital zircon grains in the analyzed samples.

	Sample	YSG	YPP	YC1σ (2+)[a]	YC2σ (3+)[a]
	AS391	251.4 ± 2.9	435	414.1 ± 3.3 (2)	418.7 ± 3.9 (3)
	AS397	355.0 ± 3.9	430	357.7 ± 3.7 (4)	360.0 ± 3.8 (5)
M1	AS405	358.3 ± 5.1	435	423.2 ± 4.9 (6)	423.3 ± 5.1 (10)
	AS420	394.7 ± 4.3	435	415.8 ± 5.1 (2)	423.6 ± 4.8 (8)
	AS423	414.4 ± 3.8	425	417.5 ± 4.2 (4)	424.6 ± 4.6 (13)

YSG: youngest single grain age; YPP: youngest graphical age peak; YC1σ (2+): youngest 1σ grain cluster; YC2σ (3+): youngest 2σ grain cluster. a: Numbers of grain ages in clusters in parentheses. Bolds are samples of this work. The calculation method can be seen in Dickinson and Gehrels, 2009.

Highlights

Ailaoshan-Song Ma-Song Chay ophiolitic mélanges have strike-parallel heterogeneity.
NW segment of Ailaoshan ophiolitic mélange shows strike-perpendicular heterogeneity.
Geometry of ophiolitic mélanges zone due to RRF sinistral strike-slip deformation.

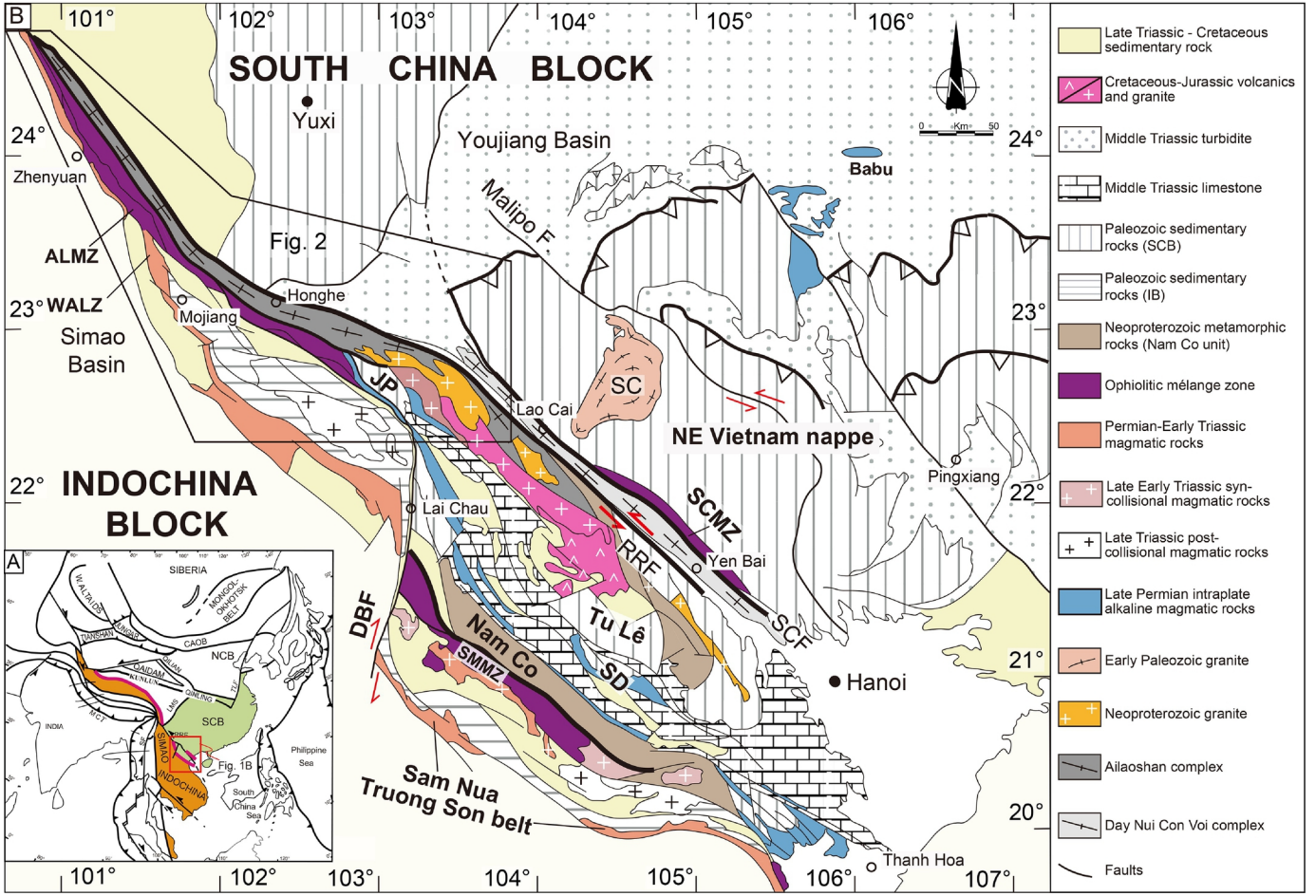
B
101°
102°
103°
104°
105°
106°
SOUTH CHINA BLOCK
Yuxi
Youjiang Basin
Babu
24°
Zhenyuan
ALMZ
Fig. 2
Malipo F.
23° WALZ
Honghe
Mojiang
Simao Basin
JP
SC
Lao Cai
NE Vietnam nappe
Pingxiang
22° INDOCHINA BLOCK
Lai Chau
SCMZ
RRF
Yen Bai
SCF
DBF
Nam Co
SMMZ
Tu Lê
SD
Hanoi
21°
Sam Nua
Truong Son belt
Thanh Hoa
20°
107°
A
SIBERIA
NCB
CAOB
SCB
INDIA
Philippine Sea
South China Sea
Fig. 1B
0 Km 50
Late Triassic - Cretaceous sedimentary rock
Cretaceous-Jurassic volcanics and granite
Middle Triassic turbidite
Middle Triassic limestone
Paleozoic sedimentary rocks (SCB)
Paleozoic sedimentary rocks (IB)
Neoproterozoic metamorphic rocks (Nam Co unit)
Ophiolitic mélange zone
Permian-Early Triassic magmatic rocks
Late Early Triassic syn-collisional magmatic rocks
Late Triassic post-collisional magmatic rocks
Late Permian intraplate alkaline magmatic rocks
Early Paleozoic granite
Neoproterozoic granite
Ailaoshan complex
Day Nui Con Voi complex
Faults

Figure 1

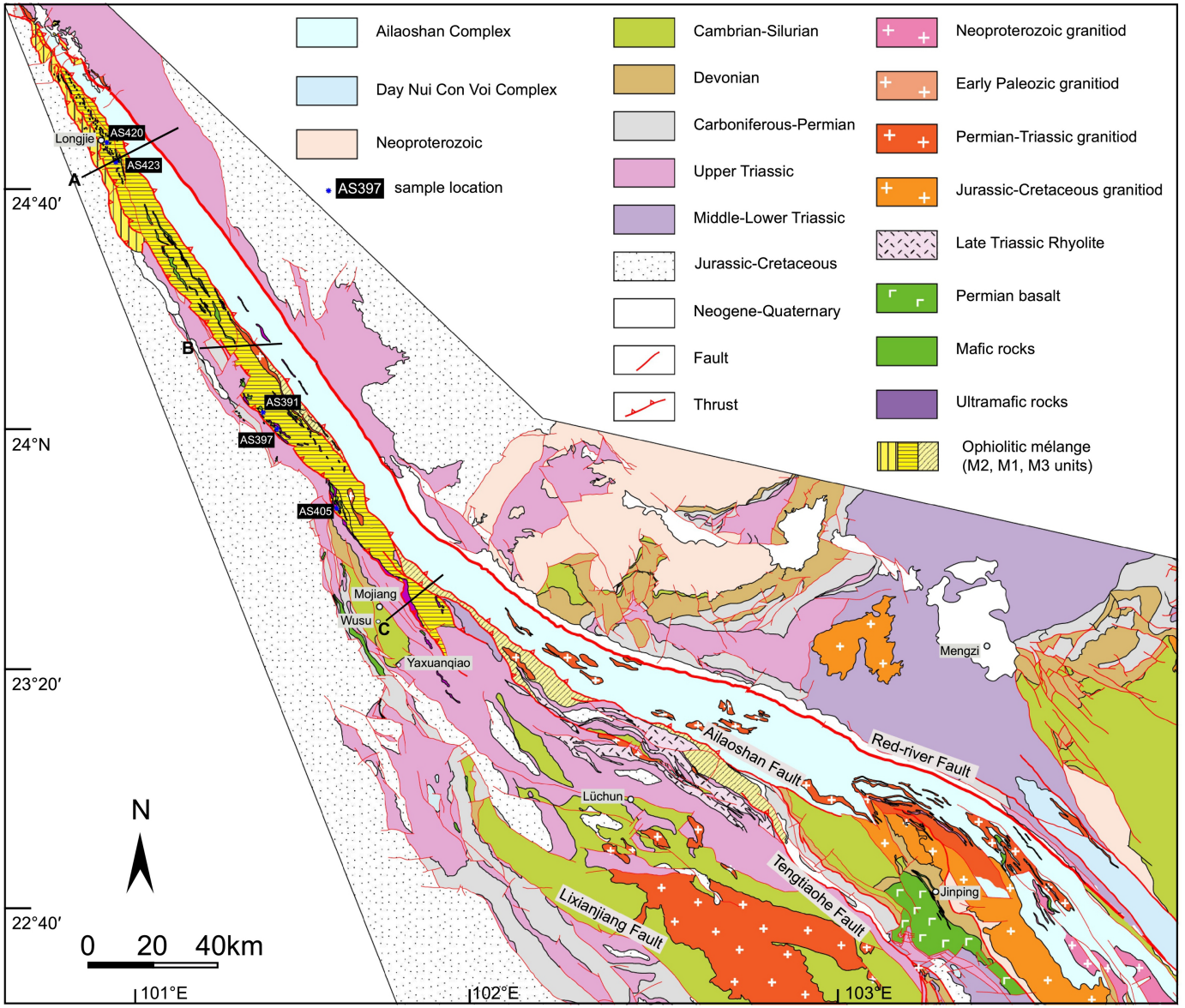
Ailaoshan Complex
Day Nui Con Voi Complex
Neoproterozoic
AS397 sample location
Cambrian-Silurian
Devonian
Carboniferous-Permian
Upper Triassic
Middle-Lower Triassic
Jurassic-Cretaceous
Neogene-Quaternary
Fault
Thrust
Neoproterozoic granitiod
Early Paleozic granitiod
Permian-Triassic granitiod
Jurassic-Cretaceous granitiod
Late Triassic Rhyolite
Permian basalt
Mafic rocks
Ultramafic rocks
Ophiolitic mélange (M2, M1, M3 units)
Longjie
AS420
AS423
A
B
AS391
AS397
AS405
Mojiang
Wusu
C
Yaxuanqiao
Mengzi
Ailaoshan Fault
Red-river Fault
Lüchun
Tengtiaohe Fault
Lixianjiang Fault
Jinping
24°40′
24°N
23°20′
22°40′
N
0 20 40km
101°E
102°E
103°E

Figure 2

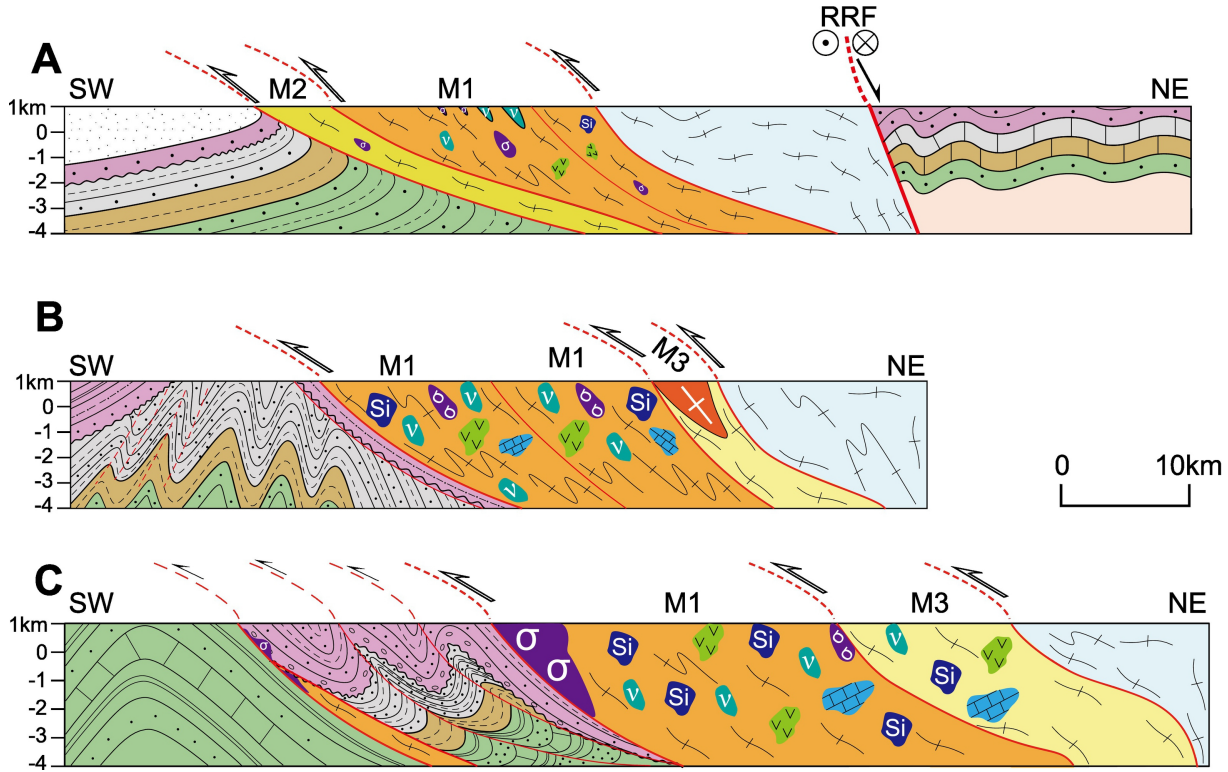
A
SW
M2
M1
RRF
NE
1km
0
-1
-2
-3
-4
B
SW
M1
M1
M3
NE
1km
0
-1
-2
-3
-4
Si
0
10km
C
SW
M1
M3
NE
1km
0
-1
-2
-3
-4
Si

Figure 3

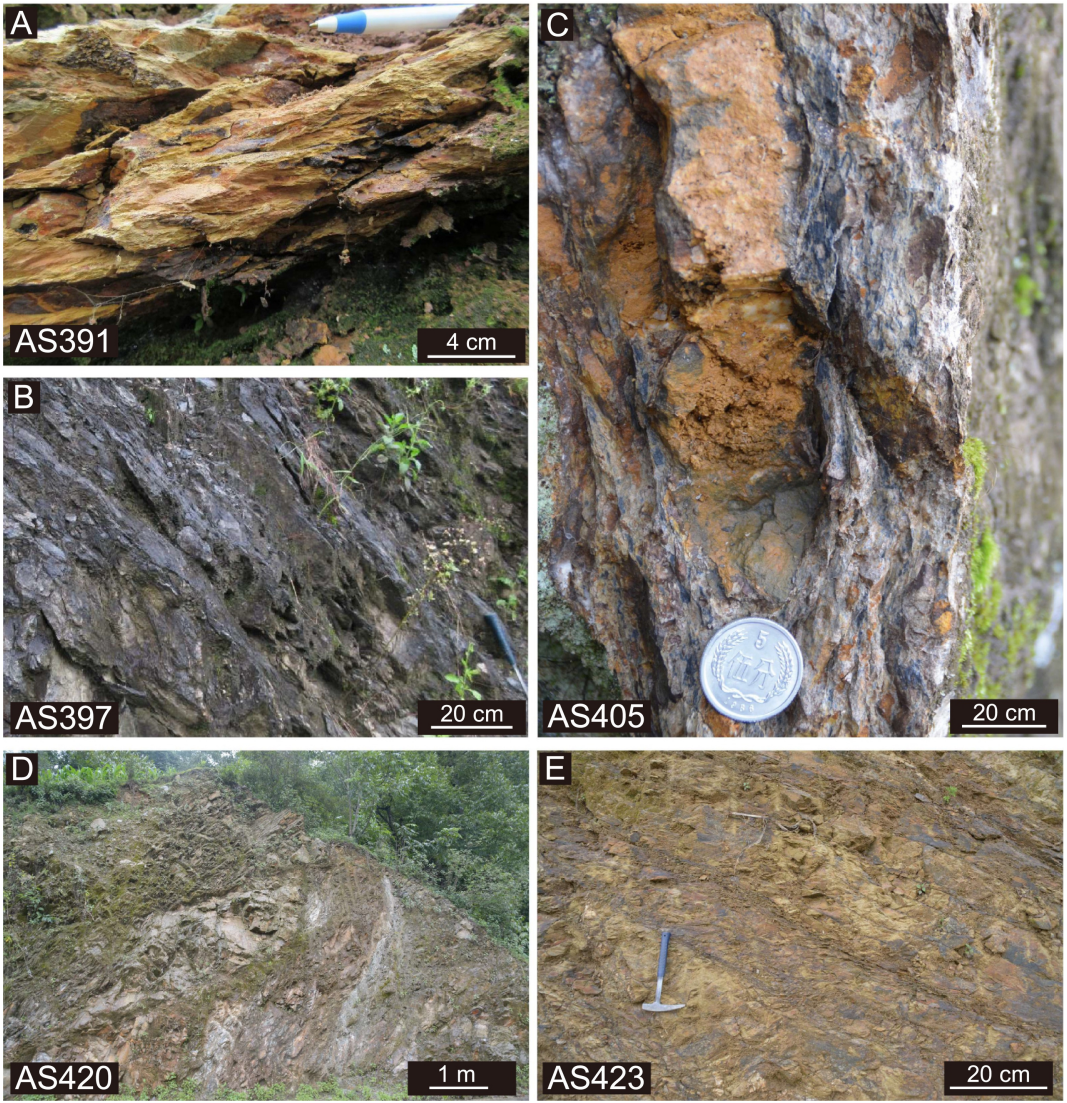

Figure 4

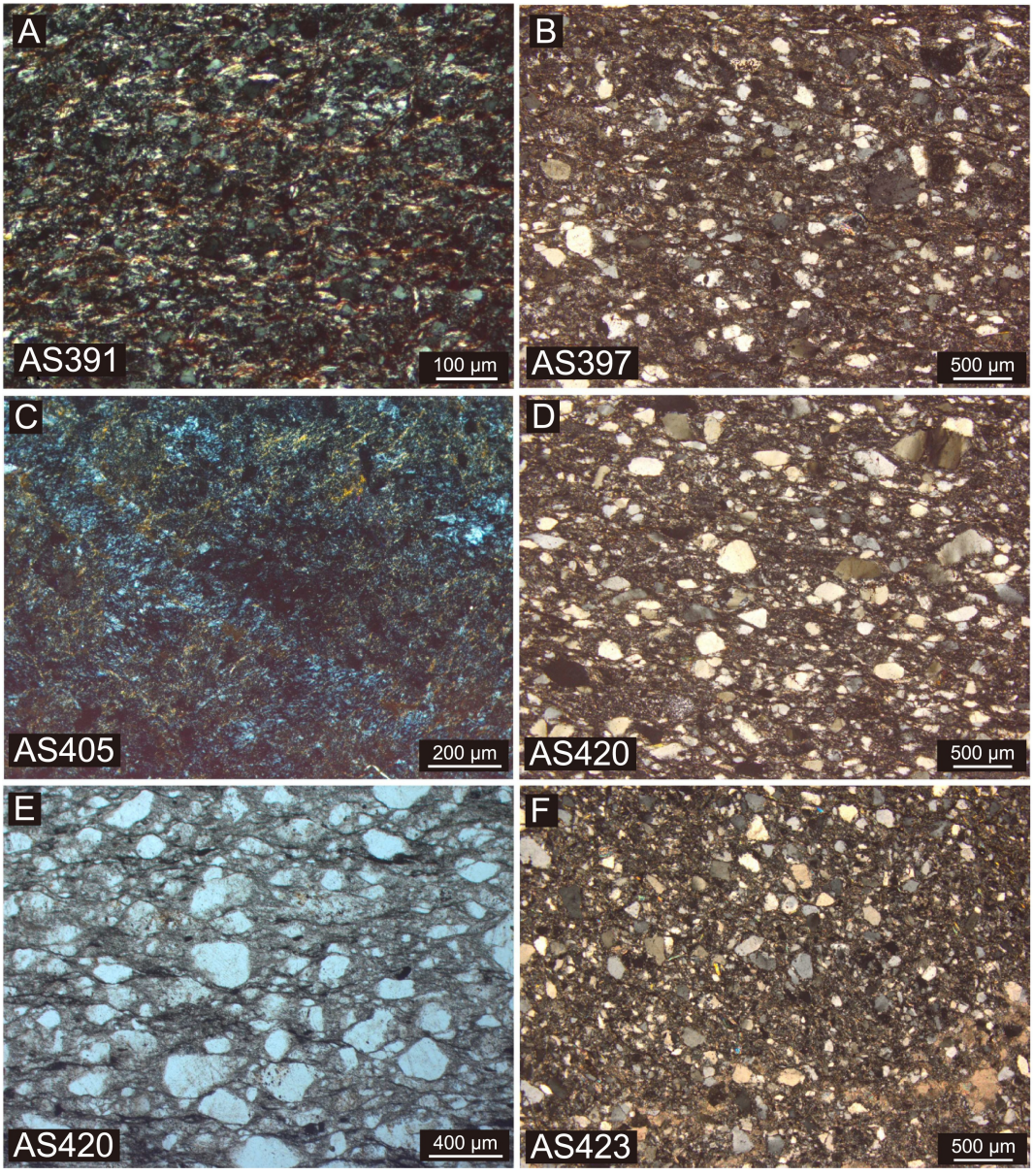
A
AS391
100 µm
B
AS397
500 µm
C
AS405
200 µm
D
AS420
500 µm
E
AS420
400 µm
F
AS423
500 µm

Figure 5

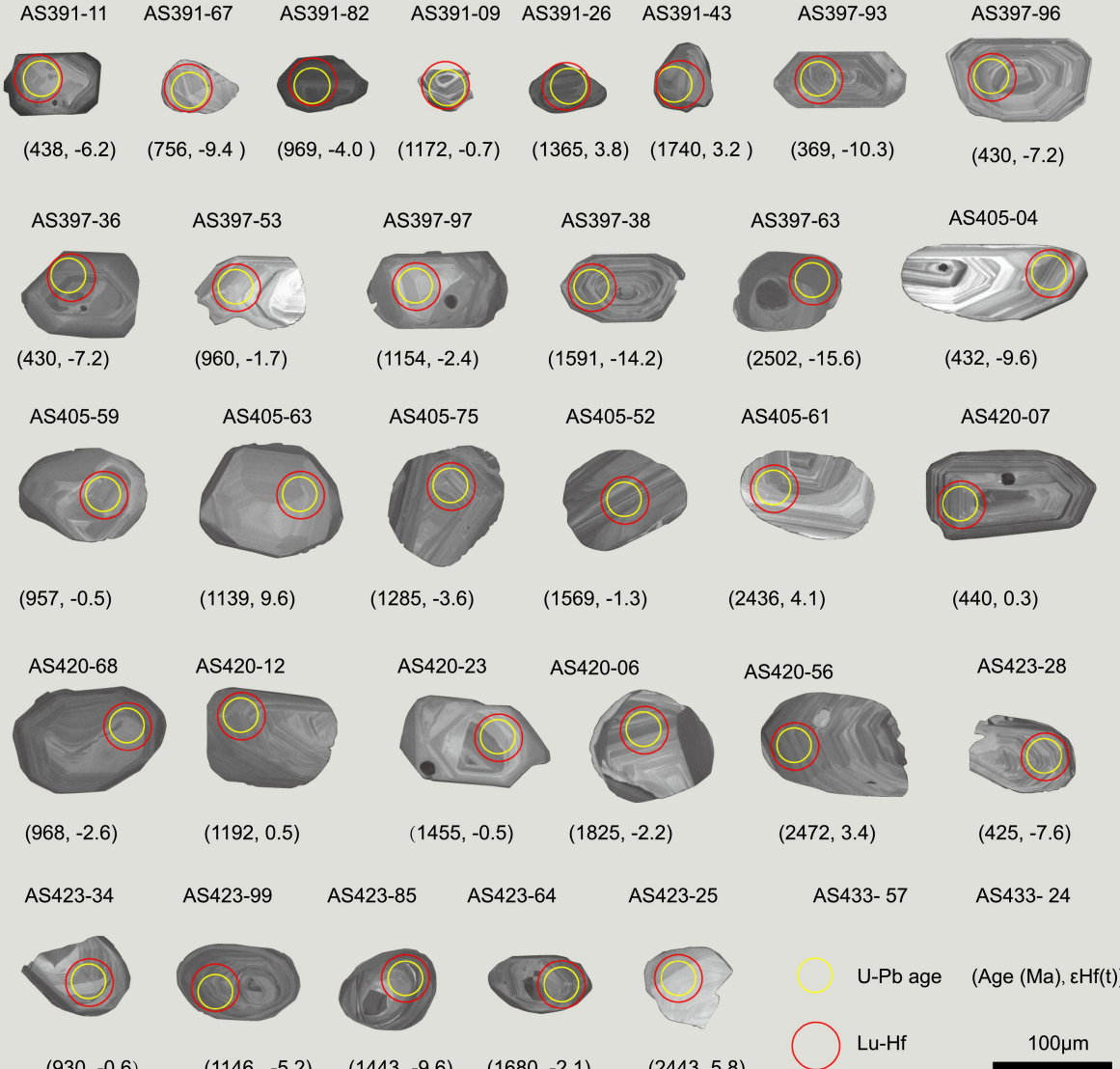
AS391-11
AS391-67
AS391-82
AS391-09
AS391-26
AS391-43
AS397-93
AS397-96
(438, -6.2)
(756, -9.4)
(969, -4.0)
(1172, -0.7)
(1365, 3.8)
(1740, 3.2)
(369, -10.3)
(430, -7.2)
AS397-36
AS397-53
AS397-97
AS397-38
AS397-63
AS405-04
(430, -7.2)
(960, -1.7)
(1154, -2.4)
(1591, -14.2)
(2502, -15.6)
(432, -9.6)
AS405-59
AS405-63
AS405-75
AS405-52
AS405-61
AS420-07
(957, -0.5)
(1139, 9.6)
(1285, -3.6)
(1569, -1.3)
(2436, 4.1)
(440, 0.3)
AS420-68
AS420-12
AS420-23
AS420-06
AS420-56
AS423-28
(968, -2.6)
(1192, 0.5)
(1455, -0.5)
(1825, -2.2)
(2472, 3.4)
(425, -7.6)
AS423-34
AS423-99
AS423-85
AS423-64
AS423-25
AS433- 57
AS433- 24
(930, -0.6)
(1146, -5.2)
(1443, -9.6)
(1680, -2.1)
(2443, 5.8)
U-Pb age
(Age (Ma), εHf(t))
Lu-Hf
100μm

Figure 6

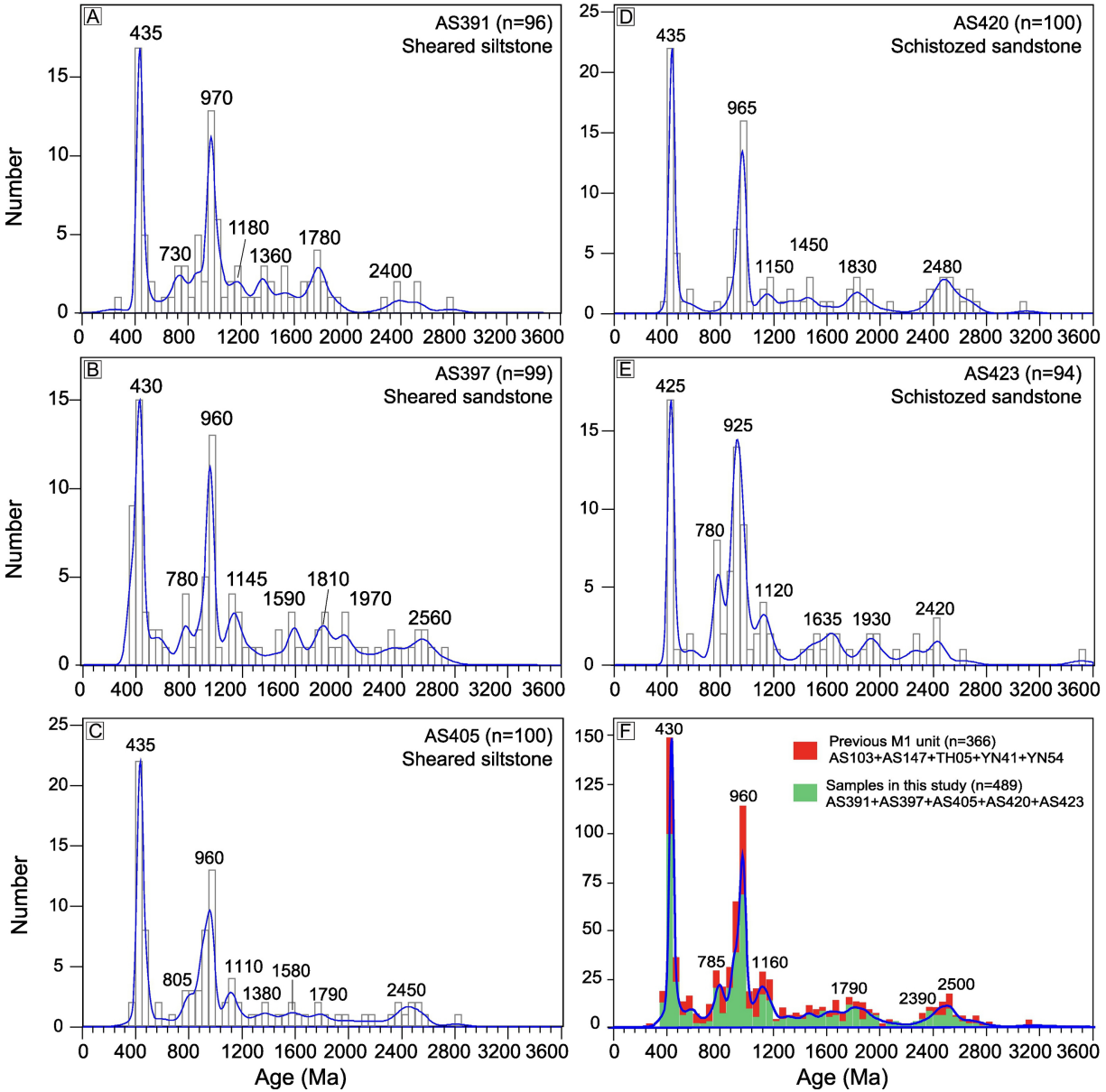
A
AS391 (n=96)
Sheared siltstone
435
970
730
1180
1360
1780
2400
D
AS420 (n=100)
Schistozed sandstone
435
965
1150
1450
1830
2480
B
AS397 (n=99)
Sheared sandstone
430
960
780
1145
1590
1810
1970
2560
E
AS423 (n=94)
Schistozed sandstone
425
925
780
1120
1635
1930
2420
C
AS405 (n=100)
Sheared siltstone
435
960
805
1110
1380
1580
1790
2450
F
Previous M1 unit (n=366)
AS103+AS147+TH05+YN41+YN54
Samples in this study (n=489)
AS391+AS397+AS405+AS420+AS423
430
960
785
1160
1790
2390
2500
Number
Age (Ma)

Figure 7

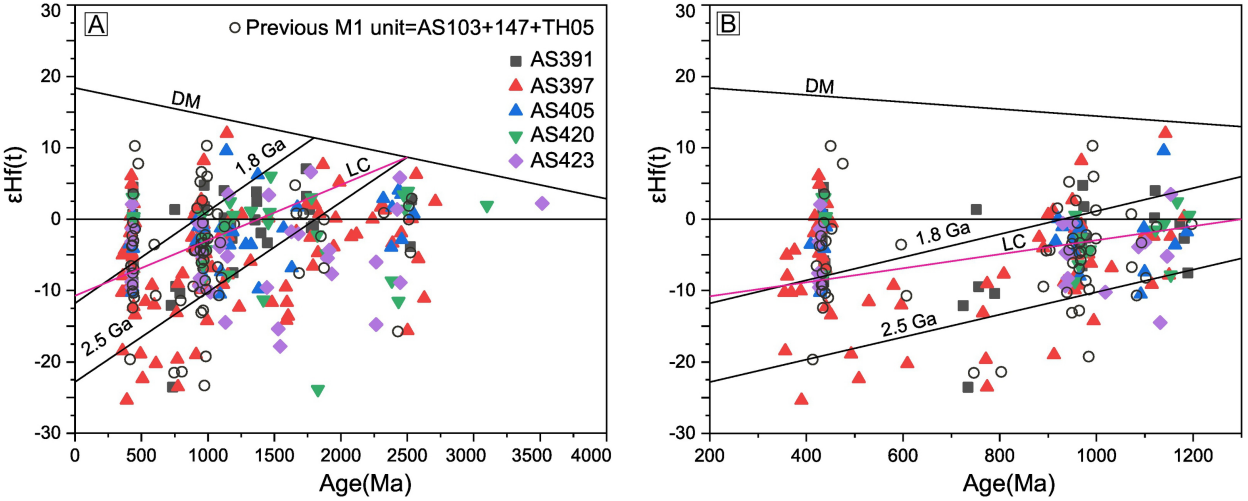
A
Previous M1 unit=AS103+147+TH05
AS391
AS397
AS405
AS420
AS423
DM
1.8 Ga
LC
2.5 Ga
εHf(t)
Age(Ma)
B
DM
1.8 Ga
LC
2.5 Ga
εHf(t)
Age(Ma)

Figure 8

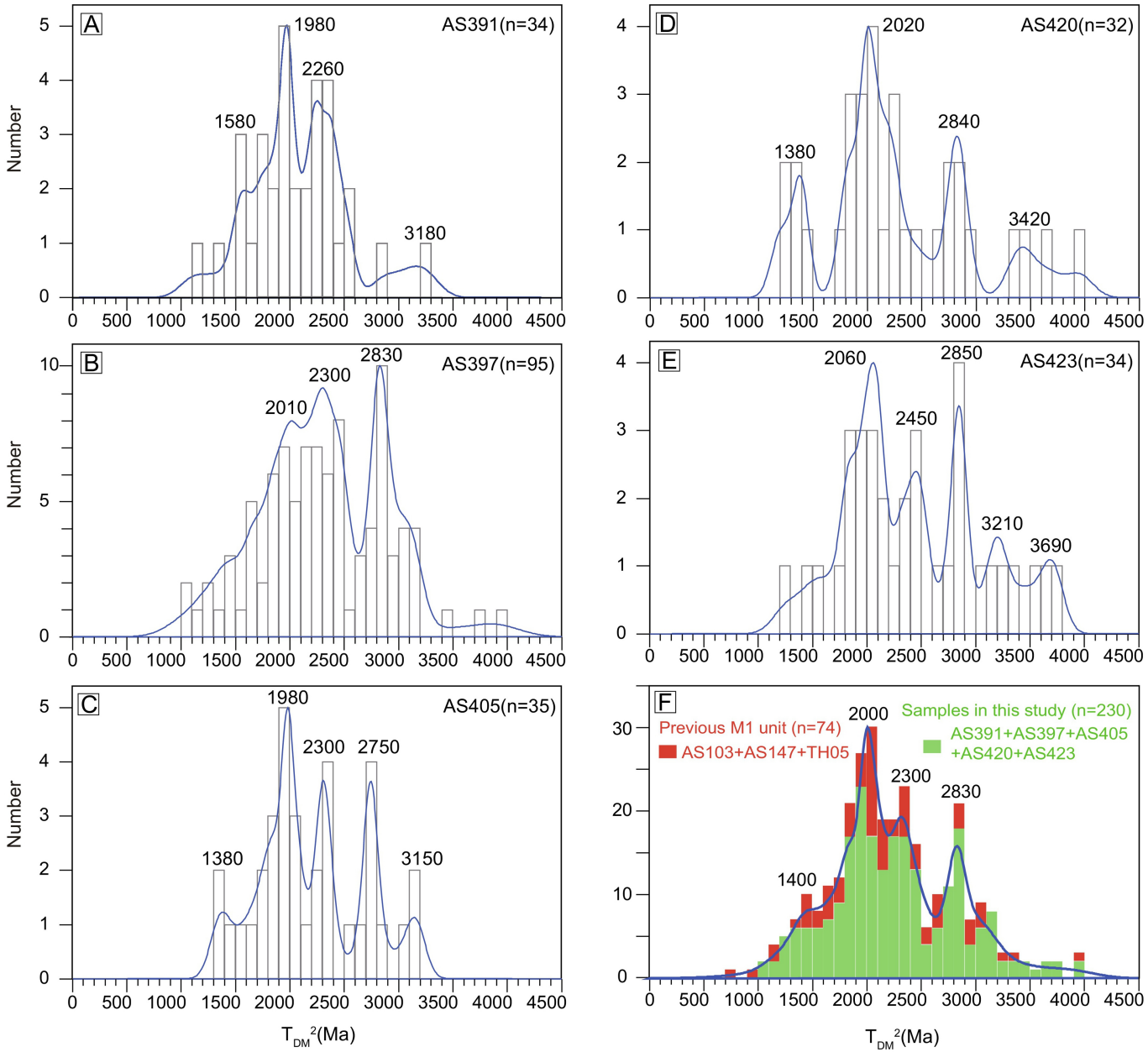
A
AS391(n=34)
1980
2260
1580
3180
B
AS397(n=95)
2830
2300
2010
C
AS405(n=35)
1980
2300
2750
1380
3150
D
AS420(n=32)
2020
2840
1380
3420
E
AS423(n=34)
2060
2850
2450
3210
3690
F
Previous M1 unit (n=74)
AS103+AS147+TH05
Samples in this study (n=230)
AS391+AS397+AS405
+AS420+AS423
2000
2300
2830
1400
Number
T_{DM}^{2}(Ma)

Figure 9

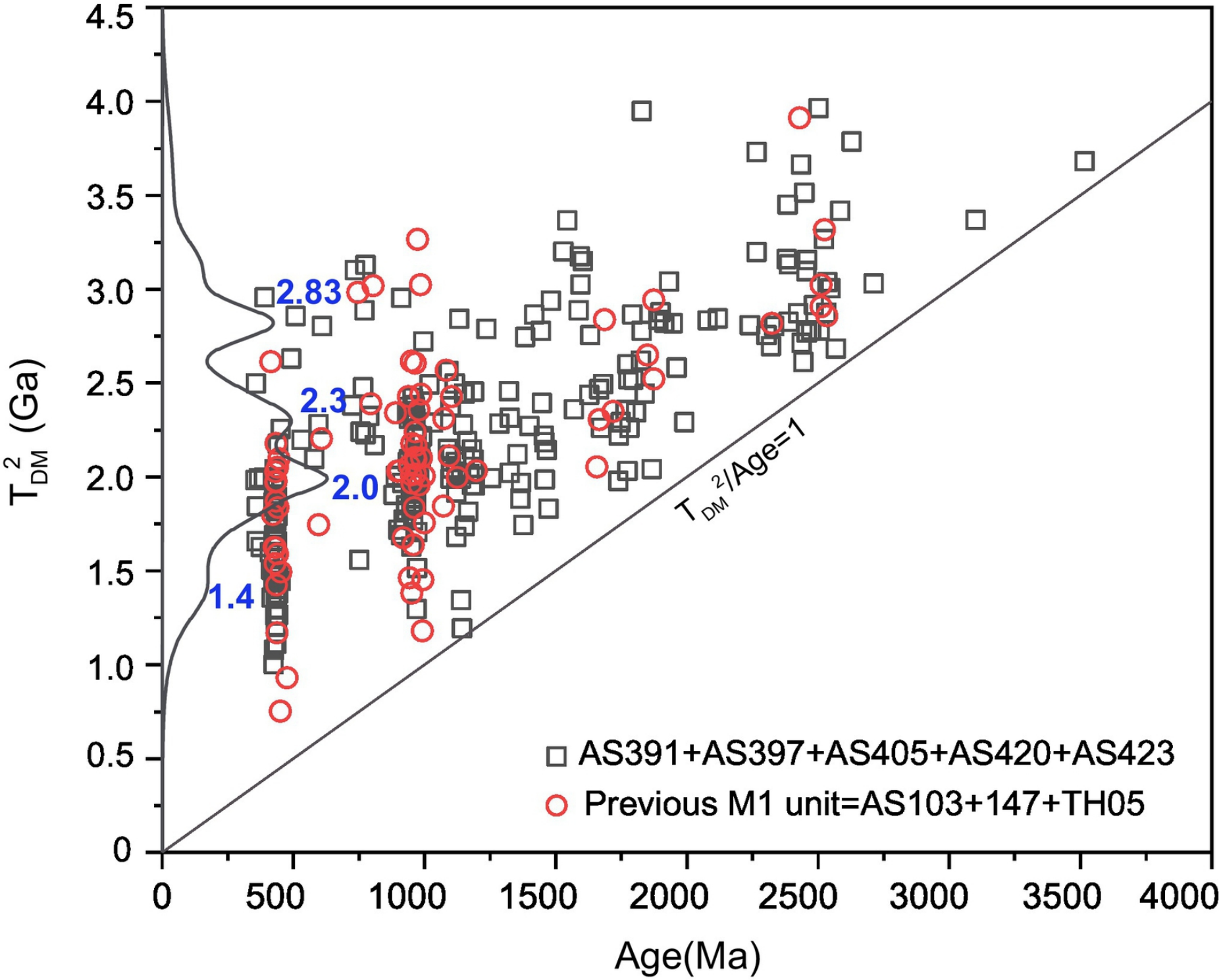
4.5
4.0
3.5
3.0
2.5
2.0
1.5
1.0
0.5
0
T_{DM}^{2} (Ga)
2.83
2.3
2.0
1.4
T_{DM}^{2}/Age=1
AS391+AS397+AS405+AS420+AS423
Previous M1 unit=AS103+147+TH05
0
500
1000
1500
2000
2500
3000
3500
4000
Age(Ma)

Figure 10

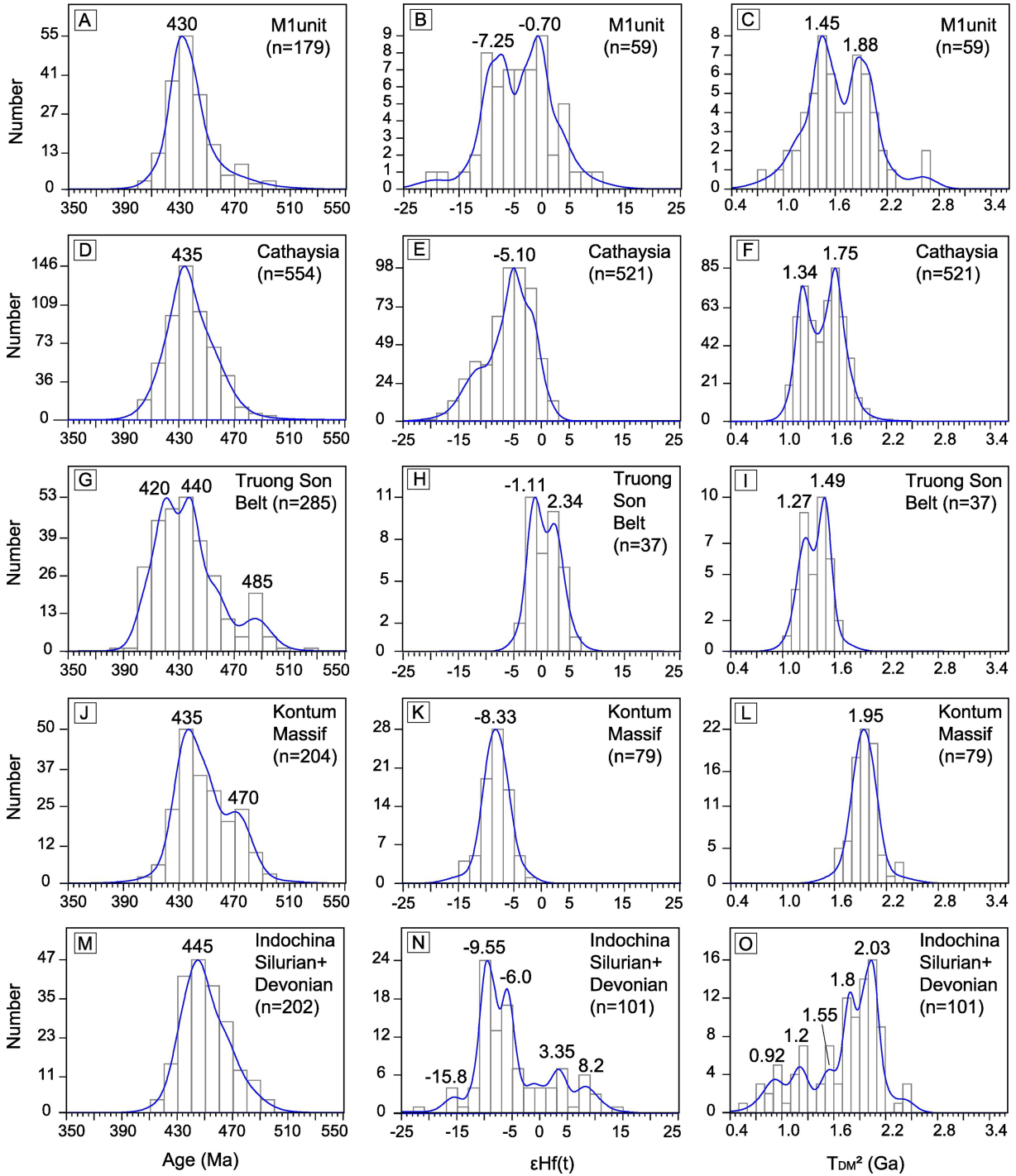
A
430
M1unit
(n=179)
B
-7.25
-0.70
M1unit
(n=59)
C
1.45
1.88
M1unit
(n=59)
D
435
Cathaysia
(n=554)
E
-5.10
Cathaysia
(n=521)
F
1.34
1.75
Cathaysia
(n=521)
G
420
440
485
Truong Son
Belt (n=285)
H
-1.11
2.34
Truong
Son
Belt
(n=37)
I
1.27
1.49
Truong Son
Belt (n=37)
J
435
470
Kontum
Massif
(n=204)
K
-8.33
Kontum
Massif
(n=79)
L
1.95
Kontum
Massif
(n=79)
M
445
Indochina
Silurian+
Devonian
(n=202)
N
-15.8
-9.55
-6.0
3.35
8.2
Indochina
Silurian+
Devonian
(n=101)
O
0.92
1.2
1.55
1.8
2.03
Indochina
Silurian+
Devonian
(n=101)
Number
Age (Ma)
εHf(t)
TDM² (Ga)

Figure 11

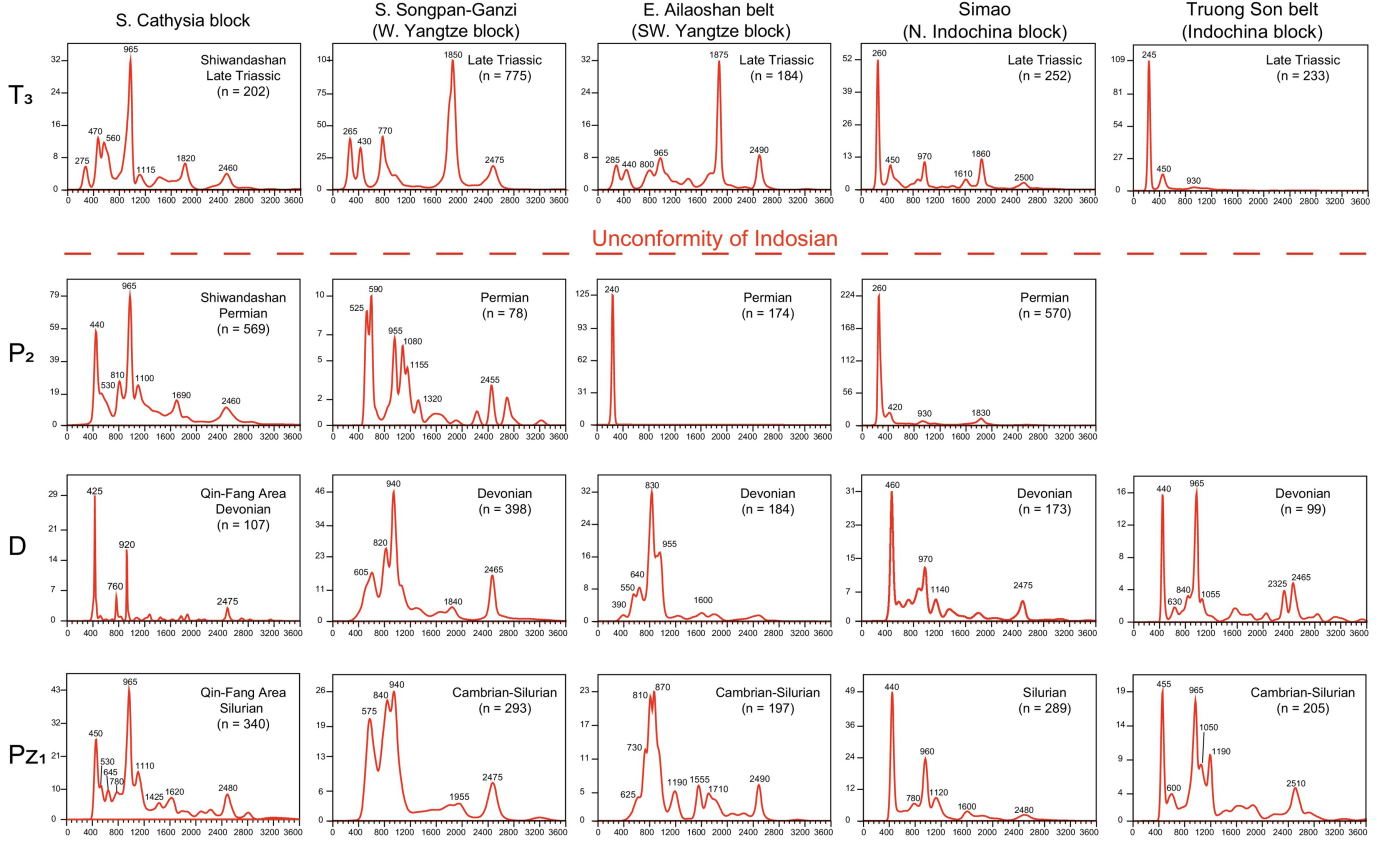
S. Cathysia block
S. Songpan-Ganzi (W. Yangtze block)
E. Ailaoshan belt (SW. Yangtze block)
Simao (N. Indochina block)
Truong Son belt (Indochina block)
T3
P2
D
PZ1
Shiwandashan Late Triassic (n = 202)
Late Triassic (n = 775)
Late Triassic (n = 184)
Late Triassic (n = 252)
Late Triassic (n = 233)
Unconformity of Indosian
Shiwandashan Permian (n = 569)
Permian (n = 78)
Permian (n = 174)
Permian (n = 570)
Qin-Fang Area Devonian (n = 107)
Devonian (n = 398)
Devonian (n = 184)
Devonian (n = 173)
Devonian (n = 99)
Qin-Fang Area Silurian (n = 340)
Cambrian-Silurian (n = 293)
Cambrian-Silurian (n = 197)
Silurian (n = 289)
Cambrian-Silurian (n = 205)

Figure 12

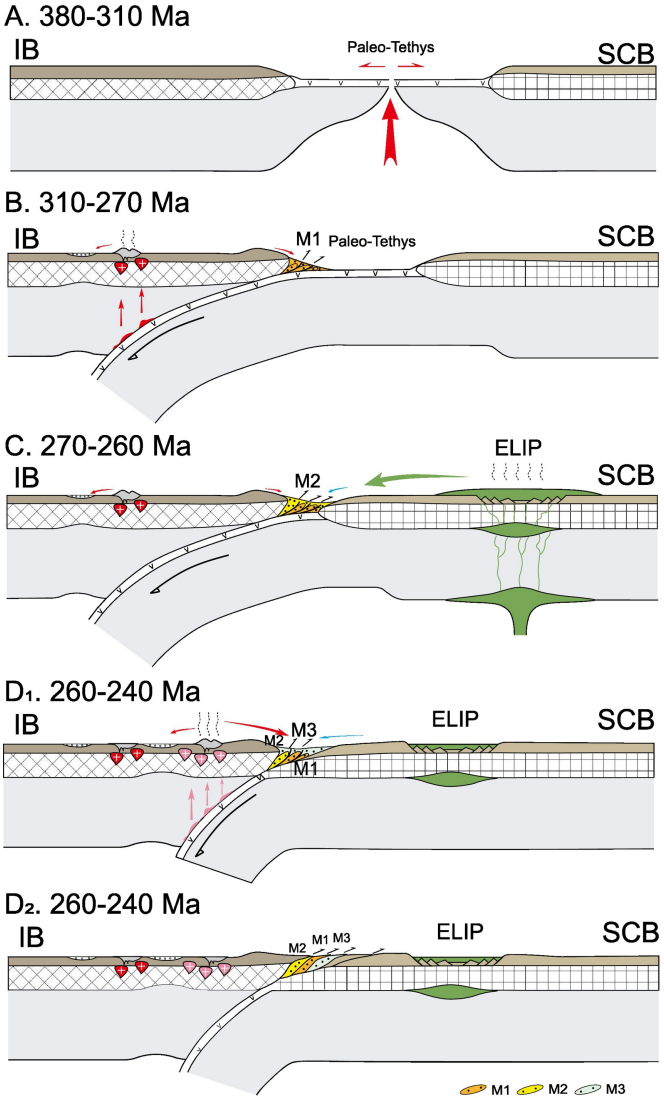
A. 380-310 Ma
IB
Paleo-Tethys
SCB
B. 310-270 Ma
IB
M1
Paleo-Tethys
SCB
C. 270-260 Ma
ELIP
IB
M2
SCB
D₁. 260-240 Ma
IB
M3
M2
M1
ELIP
SCB
D₂. 260-240 Ma
IB
M2
M1
M3
ELIP
SCB
M1
M2
M3
E. 40-18 Ma
Ailaoshan Complex
IB
M2
M1
M3
SCB

Figure 13